

CHEMICAL CARTOGRAPHY. II. THE ASSEMBLY HISTORY OF THE GALACTIC STELLAR HALO TRACED BY CARBON-ENHANCED METAL-POOR STARS

YOUNG SUN LEE¹, TIMOTHY C. BEERS², AND YOUNG KWANG KIM¹

Draft version, September 3, 2019

ABSTRACT

We present an analysis of the kinematic properties of stellar populations in the Galactic halo, making use of over 100,000 main sequence turnoff (MSTO) stars observed in the Sloan Digital Sky Survey. After dividing the Galactic halo into an inner-halo region (IHR) and outer-halo region (OHR), based on the spatial variation of carbon-to-iron ratios in the sample, we find that stars in the OHR exhibit a clear retrograde motion of -49 ± 4 km s⁻¹ and a more spherical distribution of stellar orbits, while stars in the IHR have zero net rotation (-3 ± 1 km s⁻¹) with a much more radially biased distribution of stellar orbits. Furthermore, we classify the carbon-enhanced metal-poor (CEMP) stars among the MSTO sample in each halo component into CEMP-no and CEMP-*s* sub-classes, based on their absolute carbon abundances, $A(C)$, and examine the spatial distributions and kinematics associated with each sub-class. The CEMP-no stars are the majority sub-class of CEMP stars in the OHR ($\sim 65\%$), and the minority sub-class in the IHR ($\sim 44\%$), similar to the results of several previous analyses. The CEMP-no stars in each halo region exhibit slightly higher counter-rotation than the CEMP-*s* stars, but within statistical errors. The CEMP-no stars also show a more spherical distribution of orbits than the CEMP-*s* stars in each halo region. These distinct characteristics provide strong evidence that numerous low-mass satellite galaxies (similar to the ultra-faint dwarf galaxies) have donated stars to the OHR, while more-massive dwarf galaxies provided the dominant contribution to the IHR.

Keywords: Methods: data analysis — technique: imaging spectroscopy — Galaxy: halo — stars: carbon abundances — stars: kinematics

1. INTRODUCTION

Large photometric and spectroscopic surveys such as the Sloan Digital Sky Survey (SDSS; York et al. 2000) have dramatically changed our understanding of the stellar components of the Milky Way (MW), in particular for the Galactic halo. For many years, the diffuse stellar halo of the MW was thought to consist of a single population of stars with similar kinematics, chemical abundances, and ages. However, numerous recent studies have demonstrated that the halo comprises at least two distinct stellar components (e.g., Carollo et al. 2007, 2010; de Jong et al. 2010; Beers et al. 2012; An et al. 2013, 2015; Hattori et al. 2013; Allende Prieto et al. 2014; Chen et al. 2014; Fernandez-Alvar et al. 2015, 2016, 2017; Das & Binney 2016; Janesh et al. 2016). In addition, numerical simulations of the formation of MW-like galaxies (e.g., Zolotov et al. 2009; Font et al. 2011; McCarthy et al. 2012; Tissera et al. 2013, 2014; Cooper et al. 2015) indicate that an inner/outer halo dichotomy of the Galactic halo is indeed expected.

Spatially, stars in the inner halo are predominantly located at distances up to 10 – 15 kpc from the Galactic center, whereas stars in the outer halo are mostly found in the region beyond 15 – 20 kpc. Additionally, the stellar density profile of the inner halo is flatter than that of the outer halo, which is nearly spherical. Chemically, the metallicity distribution function (MDF) of the inner-halo

stars peaks at $[Fe/H] \sim -1.6$, in contrast to the peak at $[Fe/H] \sim -2.2$ for the outer-halo stars. Kinematically, the inner-halo stars collectively exhibit essentially zero net rotation around the Galactic center, and are dominantly on high-eccentricity orbits, in contrast to the outer-halo stars, which show a net retrograde motion of about -80 km s⁻¹ and more circular orbits (Carollo et al. 2007, 2010; Kinman et al. 2012; Hattori et al. 2013). It has also been shown that the outer-halo population (OHP) is kinematically hotter than the inner-halo population (IHP), as expected (Carollo et al. 2007, 2010, 2014; An et al. 2015; Helmi et al. 2017).

However, this view (especially the interpretation of the kinematic analysis) has been challenged by Schönrich et al. (2011, 2014), who claimed that the findings by Carollo et al. (2010) may have resulted from incorrect distance assignments and selection bias of the sample. Their re-analysis of the sample used by Carollo et al. (2010) shows no retrograde motion for the OHP. Schönrich et al. (2014) further argued that the results of Carollo et al. (2007, 2010) needed to be verified after accounting for possible metallicity bias due to target selection, and to clarify whether or not the claimed retrograde motion is due to observational errors.

Meanwhile, Beers et al. (2012) refuted the arguments made by Schönrich et al. (2011), and claimed that the absence of the retrograde signal for the OHP in their analysis is in part due to their *incorrect* adoption of the relation for the distance modulus from Ivezić et al. (2008). Furthermore, they demonstrated that the retrograde signature of the OHP was detected using the proper motions alone. These dual kinematic features of the Galactic halo have also been identified based on local K-giant stars se-

¹ Department of Astronomy and Space Science, Chungnam National University, Daejeon 34134, Republic of Korea; youngsun@cnu.ac.kr

² Department of Physics and JINA Center for the Evolution of the Elements, University of Notre Dame, Notre Dame, IN 46556, USA

lected (in an entirely different manner from Carollo et al.) from the Large sky Area Multi-Object Fiber Spectroscopic Telescope (LAMOST; Cui et al. 2012) in the study of Tian et al. (2019). Additionally, many recent studies, which used *in situ* halo stars up to tens of kpc away from the Galactic center, consistently support the dichotomy of the Galactic halo (e.g., de Jong et al. 2010; Deason et al. 2011; An et al. 2013, 2015; Kafle et al. 2013, 2017; Allende Prieto et al. 2014; Chen et al. 2014; Fernandez-Alvar et al. 2015; Das & Binney 2016).

Since chemical-abundance ratios of individual stars are closely related to their star-formation history (in particular to that of the galactic fragments in which they were born), they provide valuable complimentary information for assessing the assembly history of the MW. There have been several previous efforts to understand the origin of the dichotomy of the Galactic halo using the abundances of chemical elements other than iron, such as Ca and Mg, the so called α -elements (e.g., Gratton et al. 2003; Jonsell et al. 2005; Ishigaki et al. 2010; Nissen & Schuster 2010, 2011; Fernandez-Alvar et al. 2015, 2016, 2017). These studies attempt to relate $[\alpha/\text{Fe}]$ to stellar kinematics or stellar distances, and characterize the observed trends.

Recently, carbon has emerged as valuable element to study the origin of the duality of the Galactic halo. Especially, the so-called carbon-enhanced metal-poor (CEMP; Beers & Christlieb 2005) stars have been recognized as an important tracer of the assembly history of the MW, owing to the variety of their sub-classes, which can be associated with progenitor stars of different masses.

CEMP stars, which are typically defined by $[\text{Fe}/\text{H}] \leq -1.0$ and $[\text{C}/\text{Fe}] \geq +1.0$ (or $+0.7$, depending on the study), can be divided into four major categories — CEMP-no, CEMP-*s*, CEMP-*r*, and CEMP-*r/s*, according to the level of enhancement of their neutron-capture elements (Beers & Christlieb 2005). CEMP-no stars exhibit no over-abundances of heavy neutron-capture elements, while CEMP-*s* stars have enhancements of the *s*-process (slow neutron-capture process) elements, such as Ba. CEMP-*r* stars show strong enhancements of *r*-process (rapid neutron-capture process) elements, such as Eu. Carbon-rich stars with enhancements of both the *r*-process and the *s*-process are classified as CEMP-*r/s* stars. Recently, evidence has been presented that the CEMP-*r/s* sub-class is more likely associated with a proposed intermediate neutron-capture process, the “*i*-process (intermediate neutron-capture process)”; thus CEMP-*r/s* stars are more appropriately called CEMP-*i* stars (Hampel et al. 2016).

CEMP-*s* and CEMP-no stars account for more than 90% of known CEMP stars. CEMP-*s* stars predominantly have $[\text{Fe}/\text{H}] > -2.5$, while most CEMP-no stars have $[\text{Fe}/\text{H}] < -2.5$. (e.g., Aoki et al. 2007; Yoon et al. 2016). Long-term radial-velocity monitoring of CEMP stars (e.g., Starkenburg et al. 2014; Hansen et al. 2016a,b; Jorissen et al. 2016) has shown that the binary fraction of CEMP-*s* stars is $\sim 82\%$ (including CEMP-*r/s* or CEMP-*i* stars), while the fraction of CEMP-no stars is only $\sim 17\%$, indicating that their origin is not causally connected to binary membership. Rather, their distinctive chemical-abundance patterns indicate likely pollution of their natal clouds by the first generations of massive stars.

In addition, several studies report, based on large numbers of CEMP stars, that the fraction of CEMP stars dramatically increases with decreasing metallicity (e.g., Rossi et al. 1999; Lucatello et al. 2006; Lee et al. 2013; Yong et al. 2013; Placco et al. 2014), as well as with increasing distance from the Galactic plane (Frebel et al. 2006; Carollo et al. 2012; Beers et al. 2017). This latter result is difficult to reconcile with a single-component Galactic halo. Carollo et al. (2012) argued that there is a higher frequency of CEMP stars associated with the OHP than with the IHP, based on a kinematic separation of these populations. Furthermore, Carollo et al. (2014) claimed, from an analysis of a small sample of CEMP stars with available high-resolution spectroscopy, that the OHP exhibits a relatively higher fraction of CEMP-no stars than the IHP, whereas the IHP has a similar fraction of the two sub-classes, indicative of differences in the star-formation histories of the outer-halo and inner-halo populations.

One drawback of most previous studies is that the stars used predominantly explore the Solar Neighborhood. To overcome this limitation, Lee et al. (2017) (Paper I hereafter) made use of main-sequence turnoff (MSTO) stars, with distances extending up to 15 kpc from the Galactic plane, to investigate the chemical nature of the Galactic halo system *in situ*. Paper I demonstrated that, based on $[\text{C}/\text{Fe}]$ (“carbonicity”) alone, the stellar populations of the MW halo can be readily distinguished. The component associated with the IHP shows a metallicity peak at $[\text{Fe}/\text{H}] \sim -1.5$, while the metallicity associated with the OHP peaks at $[\text{Fe}/\text{H}] \sim -2.2$, in agreement with studies by Carollo et al. (2007, 2010) and An et al. (2013, 2015), who employed completely different approaches to distinguish the populations.

Furthermore, Paper I quantitatively estimated the fraction of CEMP-no and CEMP-*s* stars in the outer-halo region (OHR) and inner-halo region (IHR), classified on the basis of their derived $A(\text{C})$ ³, and reported that the stars in the OHR exhibit a higher proportion of CEMP-no stars compared to CEMP-*s* stars, in contrast to the similar fractions of CEMP-no and CEMP-*s* stars in the IHR, consistent with results from previous, more-local studies.

Yoon et al. (2018) carried out a study similar to Paper I. They constructed a carbonicity map, using $\sim 58,000$ stars, which dominantly consists of MSTO stars in the Southern Hemisphere observed by the AAOmega Evolution of Galactic Structure (AEGIS) survey, and identify the inner- and outer-halo regions based on this map. Their results are commensurate with those from Paper I — an increasing level of $[\text{C}/\text{Fe}]$ from the IHR to the OHR, and larger numbers of CEMP-no stars and CEMP-*s* stars associated with the OHR and IHR, respectively.

In this study, the second paper in the “Chemical Cartography” series, we explore the kinematics of the Galactic halo populations, separated on the basis of their different levels of carbonicity, making use of the $\sim 105,700$ MSTO stars from SDSS used in Paper I. Note that our

³ The conventional notation is used, $A(\text{C}) = \log \epsilon(\text{C}) = \log (N_{\text{C}}/N_{\text{H}}) + 12$, and is calculated from medium-resolution spectroscopy using $A(\text{C}) = [\text{C}/\text{Fe}] + [\text{Fe}/\text{H}] + A(\text{C})_{\odot}$, where we adopt the Solar abundance of carbon from Asplund et al. (2009), $A(\text{C})_{\odot} = 8.43$.

approach differs from many previous studies, which identified halo populations by their kinematic and orbital properties, in that we use the distinctive carbonicity signature to carry out the division, then consider the resulting kinematics.

This paper is arranged as follows. Section 2 briefly summarizes the sample selection of the MSTO stars, and describes the derivation of the quantities used for the kinematic analysis, as well as our division of the Galactic halo regions and classification of CEMP-*s* and CEMP-no stars. In Section 3, we discuss the potential impact of the target-selection bias present in our MSTO sample on the identification of the Galactic halo regions, and explore the existence of the systematic offsets in our adopted distance scale. Section 4 presents the distinct chemical and kinematic signatures of the stellar populations in the Galactic halo. Section 5 reports the spatial and kinematic properties of the CEMP-*s* and CEMP-no stars in each Galactic halo region, providing insight to the origin of each halo component as well as the assembly history of the MW, as discussed in Section 6. A brief summary and conclusions are provided in Section 7.

2. HALO MAIN-SEQUENCE TURNOFF STARS, KINEMATIC CALCULATIONS, AND CLASSIFICATION OF CEMP-*S* AND CEMP-NO STARS

2.1. Sample Selection

As described in detail in Paper I, in order to construct a carbonicity map, we gathered medium-resolution ($R \sim 1800$) spectra of MSTO stars from the legacy SDSS program, the Sloan Extension for Galactic Understanding and Exploration (SEGUE-1 and SEGUE-2; Yanny et al. 2009), and the Baryon Oscillation Spectroscopic Survey (BOSS; Dawson et al. 2013). Stellar atmospheric-parameter (T_{eff} , $\log g$, and $[\text{Fe}/\text{H}]$) estimates, and the carbonicity, $[\text{C}/\text{Fe}]$, were obtained from the SEGUE Stellar Parameter Pipeline (SSPP; Lee et al. 2008a,b; Allende Prieto et al. 2008; Lee et al. 2011, 2013; Smolinski et al. 2011). Paper I also validated our measurement of $[\text{C}/\text{Fe}]$, by performing various calibrations with SDSS stars in common with the sample of Yoon et al. (2016), which reports high-resolution determinations of $[\text{Fe}/\text{H}]$ and $[\text{C}/\text{Fe}]$ from the literature. As part of this effort, we adjusted for systematic offsets arising from the difficulty of detecting the CH G -band in low S/N spectra, by carrying out a noise-injection experiment over a grid of synthetic spectra. Our final sample of MSTO stars satisfies the following conditions: $15.0 \leq g_0 \leq 19.4$, $0.22 \leq (g-r)_0 \leq 0.38$, $3.5 \leq \log g \leq 4.8$, $5600 \text{ K} \leq T_{\text{eff}} \leq 6700 \text{ K}$, $S/N \geq 12$, and equivalent width of the CH- G band around 4300 \AA larger than 0.6 \AA . These criteria yielded a total of $N \sim 105,700$ stars.

One subtlety to be aware of is that we use the adopted value of $[\text{Fe}/\text{H}]$ from the SSPP, not the value determined during the estimation of $[\text{C}/\text{Fe}]$, as it exhibits a smaller offset and scatter when compared to the high-resolution results. Accordingly, we calculated $[\text{C}/\text{Fe}]_{\text{adjusted}} = [\text{C}/\text{H}] - [\text{Fe}/\text{H}]_{\text{adopted}}$, where $[\text{C}/\text{H}] = [\text{C}/\text{Fe}] + [\text{Fe}/\text{H}]$. $[\text{C}/\text{Fe}]$ and $[\text{Fe}/\text{H}]$ are the estimates from the carbon-determination routine. Throughout the remainder of this paper, we refer to $[\text{C}/\text{Fe}]_{\text{adjusted}}$ and $[\text{Fe}/\text{H}]_{\text{adopted}}$ as simply $[\text{C}/\text{Fe}]$ and $[\text{Fe}/\text{H}]$, respectively.

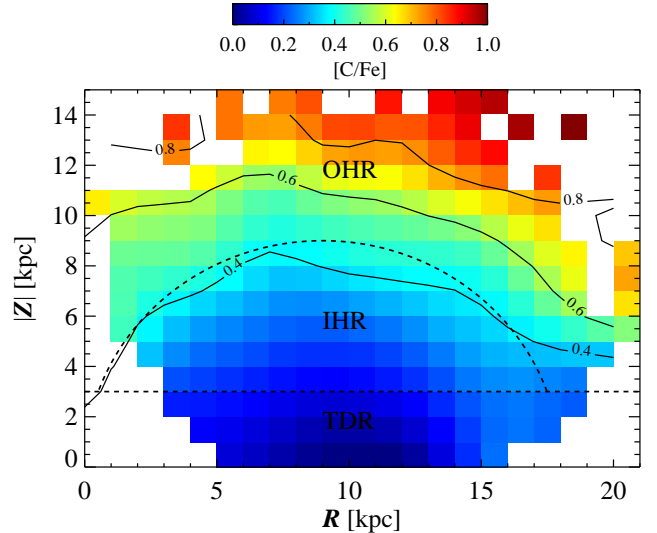


Figure 1. Map of carbonicity, $[\text{C}/\text{Fe}]$, for our MSTO sample in the $|Z|$ versus R plane, as shown in Lee et al. (2017). $|Z|$ is the absolute distance from the Galactic mid-plane, while R is the projected distance onto the plane from the Galactic center. The bin size is 1×1 kpc; each pixel contains at least three stars. Each pixel represents a median value of $[\text{C}/\text{Fe}]$, with the color scale shown in the color bar. Contours of median $[\text{C}/\text{Fe}]$ values are overplotted. The dashed line at $|Z| = 3$ kpc indicates the approximate upper boundary of a thick-disk region (TDR), while the area between the thick-disk upper limit and the dashed circle represents an inner-halo region (IHR). The area above the dashed circle is assigned to an outer-halo region (OHR). We applied a Gaussian kernel to the map to obtain a smooth spatial distribution of $[\text{C}/\text{Fe}]$. Note that each bin with $[\text{C}/\text{Fe}] > +1.0$ is forced to a value of $[\text{C}/\text{Fe}] = +1.0$, then used to construct our map for stars in the range of carbonicity $[0, +1.0]$, to better illustrate the subtle contrast in the map.

2.2. Calculations of Space Velocity Components and Orbital Parameters

The primary goal of this study is to carry out a detailed investigation of the distinct kinematic characteristics of the Galactic halo populations. Below we describe our procedures for obtaining distances, radial velocities, and proper motions for the stars in our MSTO sample.

The distance to each star was estimated following the methodology described by Beers et al. (2000, 2012), who report a typical uncertainty on the order of 15 – 20%. We computed two other distances – one from the Galactic mid-plane, represented by Z , and the other from the Galactic center projected onto the Galactic plane, denoted by R . We assumed that the Sun is located at $R_{\odot} = 8.0$ kpc from the Galactic center. We adopted the SDSS radial velocity measured by cross-correlated with the ELODIE spectral library (Prugniel & Soubiran 2001), with a typical precision of $\sim 2 \text{ km s}^{-1}$ (Allende Prieto et al. 2008).

In order to obtain the most accurate space motions for our program stars, we cross-matched the MSTO stars with *Gaia* Data Release 2 (DR2; Gaia Collaboration et al. 2018) to obtain their proper motions. Even though the typical uncertainty is less than 3.0 mas yr^{-1} for $G < 21$, we excluded from our kinematic analysis stars with errors in proper motion larger than 1.0 mas yr^{-1} .

Based on the above inputs, we first calculated the U , V , and W velocity components. We adopted $(U, V, W)_{\odot} = (-10.1, 4.0, 6.7) \text{ km s}^{-1}$ (Hogg et al. 2005) to adjust for the Solar peculiar motions with respect to the Local

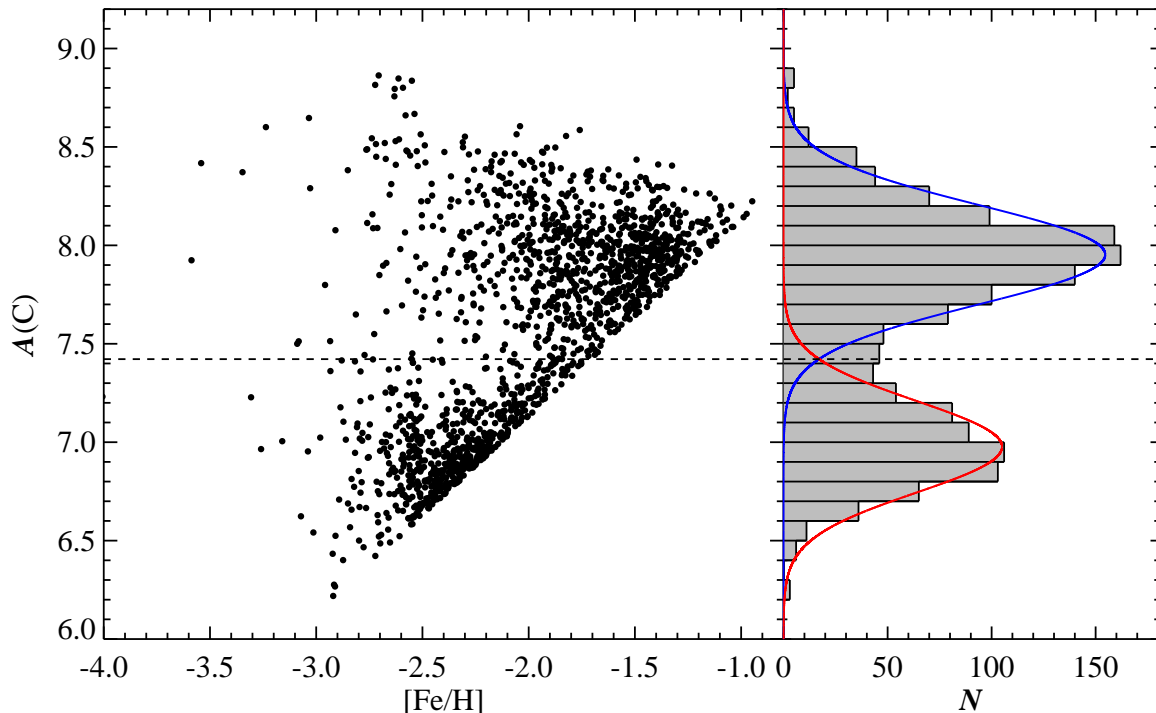


Figure 2. *Left panel:* Plot of $A(C)$ versus $[\text{Fe}/\text{H}]$. *Right panel:* Histogram of $A(C)$ values, which clearly shows a bimodal distribution. Two Gaussians, shown as red and blue curves, are fitted to the histogram. The crossing point of the two Gaussians is $A(C) = 7.42$, shown as a black dashed line. This value is used to divide our MSTO stars into low- $A(C)$ and high- $A(C)$ stars. We only considered stars with $[\text{C}/\text{Fe}] \geq +0.7$ and $S/N \geq 30$ in construction of this diagram.

Standard of Rest (LSR). For the purpose of our analysis, we computed three velocity components, V_R , V_ϕ , and V_Z in a cylindrical coordinate system centered on the Galactic center, as well as V_r , V_θ , and V_ϕ in a spherical coordinate system around the Galactic center. We assumed in these calculations that the rotation velocity of the LSR is $V_{\text{LSR}} = 220 \text{ km s}^{-1}$ (Kerr & Lynden-Bell 1986).

We adopted an analytic Stäckel-type gravitational potential (see Chiba & Beers 2000 for details) in order to compute the apo-Galacticon distance (r_{apo}), peri-Galacticon distance (r_{peri}), and stellar orbital eccentricity (e), calculated as $e = (r_{\text{apo}} - r_{\text{peri}}) / (r_{\text{apo}} + r_{\text{peri}})$. Uncertainties in the derived kinematics and orbital parameters were estimated from 100 realizations of a Monte Carlo simulation, taking into account propagation of the errors in the observed quantities.

As a check on their possible effect on our results, we adopted more recent reported values of $V_{\text{LSR}} = 236 \pm 3 \text{ km s}^{-1}$ (Kawata et al. 2019), $R_\odot = 8.2 \pm 0.1 \text{ kpc}$ (Bland-Hawthorn & Gerhard 2016), and $(U, V, W)_\odot = (-11.10, 12.24, 7.25) \text{ km s}^{-1}$ (Schönrich et al. 2010), and recomputed the velocity components and orbital parameters. We found that the mean difference between our adopted velocity components and orbital parameters and those derived with the more recent values of V_{LSR} , R_\odot , and $(U, V, W)_\odot$ is less than 1 km s^{-1} , with a scatter smaller than 5 km s^{-1} , for V_r and V_θ , and 0.4 kpc , with a scatter less than 1.2 kpc for r_{apo} . However, as might be expected, we derived a mean offset of -23 km s^{-1} , with a small scatter of 1.8 km s^{-1} , for V_ϕ . This may affect our rotational motion by about 20 km s^{-1} , although the interpretation of our results does not change much. As we

wish to compare our findings with those of previous studies, which used the older values, we have retained these for V_{LSR} , R_\odot , and $(U, V, W)_\odot$ in our analysis below.

After removing stars with large proper motion errors (or those lacking proper motion information altogether), non-physically derived orbital eccentricities, or very high ($V_\phi > 500 \text{ km s}^{-1}$) or low ($V_\phi < -500 \text{ km s}^{-1}$) rotation velocities, we obtained a sample of $N \sim 101,700$ stars for the kinematic analysis.

2.3. Division of Galactic Halo Regions

In Paper I, we constructed a so-called “carbonicity map”, as shown in Figure 1, and divided the map into four primary regions, based on the level of the carbon enhancement with respect to iron. However, since the present study aims at inspection of the kinematics of stars within the chemically divided regions, and we have a limited number of stars in the outer-halo region (due to the lack of proper motion information for these more distant stars), we redefined the map into three regions as follows:

- Thick-disk region (TDR) – The region below the straight-dashed line at $|Z| = 3 \text{ kpc}$ in Figure 1, where $|Z|$ is the absolute distance from the Galactic mid-plane. Stars in this area are dominated by the thick-disk population (TDP).
- Inner-halo region (IHR) – The area surrounded by the line of $|Z| = 3 \text{ kpc}$ and the dashed curve, which closely follows the contour line of $[\text{C}/\text{Fe}] = +0.4$. Stars in this area are dominated by the IHP.
- Outer-halo region (OHR) – The region above the dashed curve and $|Z| > 6 \text{ kpc}$. The additional con-

straint by $|Z| > 6$ kpc is to minimize overlapping populations from the IHR. Stars in this region are dominated by the OHP.

We cut the sample at $|Z| \leq 3$ kpc for the TDR after considering the scale heights of the thick disk and the metal-weak thick disk determined by [Carollo et al. \(2010\)](#). The (dashed circle) division line between the IHR and OHR is determined by inspection of the carbonicity map and the map of fractions of CEMP-*s* and CEMP-no stars, shown in the left panel of [Figure 15](#). Note that, as we removed the transition region in [Figure 1](#), the dashed curve has a radius of 9 kpc rather than 8.5 kpc as in [Paper I](#). We stress again that our strategy to separate the stellar components for the IHR and OHR is *not* based on metallicity or kinematics, but solely relies on the level of $[C/Fe]$ at a given location. These regions are shown with black labels in [Figure 1](#).

2.4. Sub-classification of the MSTO Sample into CEMP-*s* and CEMP-no Stars

As we seek to identify possible distinct kinematic differences between CEMP-*s* and CEMP-no stars of the IHR and OHR, in order to understand the origin of the dichotomy of the Galactic halo system, we first need to establish the criterion for making this separation. The conventional approach to distinguish CEMP-*s* from CEMP-no stars is to employ $[Ba/Fe]$ abundance ratios derived from high-resolution spectroscopy. Recently, however, [Yoon et al. \(2016\)](#) demonstrated that these sub-classes of CEMP stars can be equally well identified by the level of absolute carbon abundance, $A(C)$, which can be derived from medium-resolution spectroscopy. As we have no high-resolution measurements of $[Ba/Fe]$ for the MSTO stars, we applied this latter approach to sub-classify our program stars.

[Figure 2](#) illustrates the methodology we employ to distinguish CEMP-*s* stars and CEMP-no stars from CEMP stars in our MSTO sample. The right panel of this figure is the histogram of $A(C)$ values, which exhibits a clear bimodal distribution of $A(C)$. To divide the low- $A(C)$ stars, which we assign to the CEMP-no sub-class from the high- $A(C)$ stars, which we assign to the CEMP-*s* sub-class, we first fit two Gaussians to the distribution of $A(C)$. From this exercise, we identify the point where the two Gaussians cross, $A(C) = 7.42$, indicated as a black dashed line in the figure. We distinguish CEMP-no stars with $A(C) \leq 7.42$ from the CEMP-*s* stars with $A(C) > 7.42$. Note that in this exercise, we only considered stars with $[C/Fe] \geq +0.7$ with spectra having $S/N \geq 30$.

Our adopted value of $A(C) = 7.42$ differs somewhat from that of [Yoon et al. \(2016\)](#), $A(C) = 7.1$, which is derived from stars with available high-resolution spectroscopy. There are several factors that account for this discrepancy. Our MSTO sample covers substantially different ranges of metallicity, as can be seen by comparison of [Figure 2](#) with [Figure 1](#) of [Yoon et al. \(2016\)](#). Their CEMP-no stars are dominated by stars with $[Fe/H] < -3.0$, unlike our sample, which is dominated by stars with $[Fe/H] > -3.0$. In addition, their sample includes a large number of sub-giants and giants, whereas our sample of MSTO excludes these stars by definition. If we only consider the CEMP stars in their sample with

$[Fe/H] > -3.5$ and in the same temperature and gravity ranges as our sample, application of our above procedure to separate CEMP-no and CEMP-*s* stars yields a division at $A(C) = 7.2$, similar to their adopted value.

Our inability to detect low- $A(C)$ CEMP-no stars among metal-poor MSTO stars also contributes to the discrepancy. Even though we restricted our sample to rather narrow ranges of the temperature and surface gravity, the appropriate $A(C)$ division line between CEMP-no and CEMP-*s* stars probably still depends, at least weakly, on stellar temperature, luminosity class, and metallicity. Since a value of $A(C) = 7.42$ is more suitable for dividing the CEMP-no and CEMP-*s* stars in our MSTO sample, we adopted this value for our analysis. As CEMP-*r* and CEMP-*r/s* (or CEMP-*i*) stars generally exhibit relatively higher $A(C)$ values than the CEMP-no stars, we considered all CEMP stars with $A(C) > 7.42$ as CEMP-*s* stars. Stars in these sub-classes represent a small fraction of CEMP stars, in any case.

Note that, when classifying CEMP stars into the CEMP-*s* and CEMP-no sub-classes following the method described above, there exists some level of cross-contamination. However, according to [Yoon et al. \(2016\)](#), the cross-contamination fraction is less than 10%, which is very small, compared to the direct use of Ba abundances derived from high-resolution spectroscopy. In addition, there may exist degeneracy between CEMP-no and CEMP-*r* and CEMP-*s* and CEMP-*i*. However, as they are minority among CEMP stars, the contamination by these objects are negligible as well.

3. TARGET-SELECTION BIAS AND DISTANCE ERRORS

Since biases arising from the selection of spectroscopic targets in SDSS and any systematic errors in derived distances for our MSTO sample could affect our results and subsequent interpretation, in this section we examine their possible impact.

3.1. Target-Selection Bias

As the target selection for spectroscopy in SDSS was mostly carried out by application of cuts in apparent magnitude and colors, the observed stars can possibly be biased toward the inclusion of more metal-poor stars, in particular as a function of distance. In turn, this can affect the carbonicity map ([Figure 1](#)), and identification of the Galactic halo regions, hence their kinematic properties and interpretation.

In order to test the severity of this potential bias, we first obtained a sample of MSTO stars corrected for this selection bias, in order to evaluate how much it affects the underlying metallicity distribution of our MSTO sample. We followed the usual approach for deriving the selection function for our MSTO stars, as described in other studies (e.g., [Schlesinger et al. 2012](#); [Nandakumar et al. 2017](#); [Wojno et al. 2017](#); [Chen et al. 2018](#)). The basic idea is to calculate the fraction of the spectroscopically targeted stars among the photometrically available targets in a certain range of magnitude and color on a color-magnitude diagram, individually for each SDSS plug-plate. We adopted a magnitude and color bin size of 0.2 mag and 0.05 mag, respectively, for a color-magnitude diagram of r and $g - r$ for this calculation. Here, we regard the selection function as the ratio of the number of

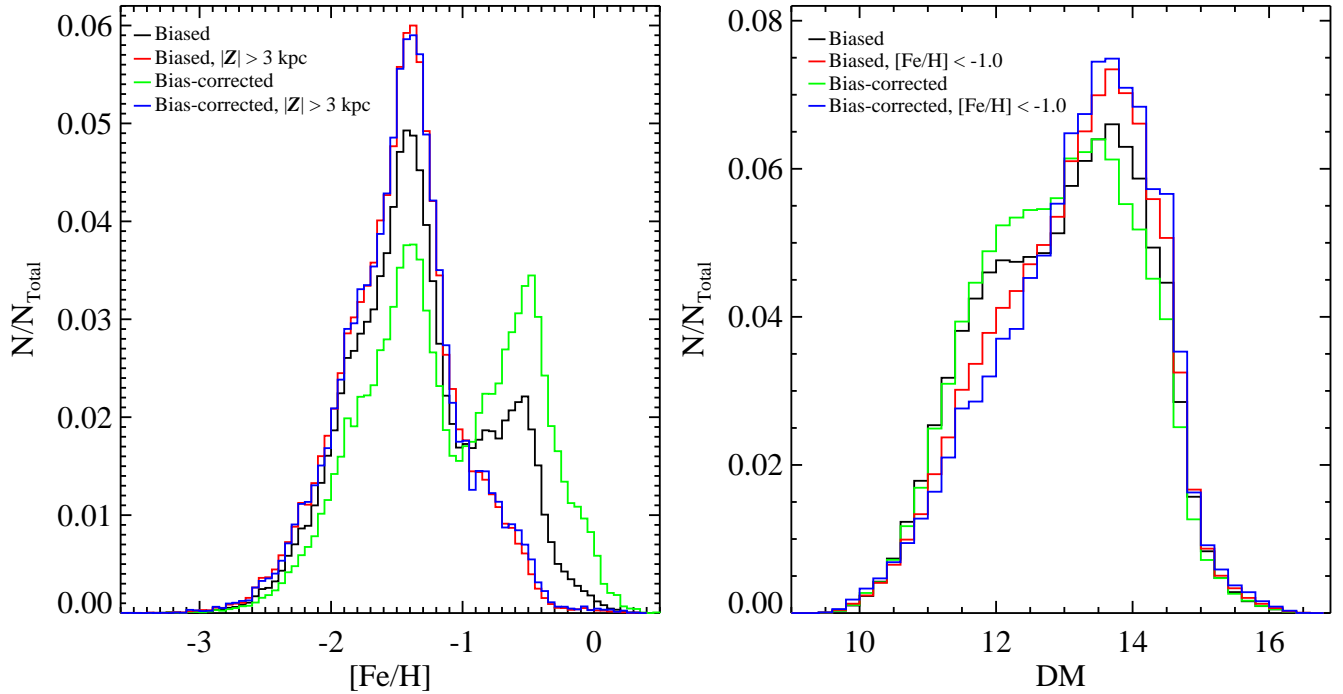


Figure 3. *Left panel:* Metallicity distribution functions for the original, target-selection biased (black and red), and bias-corrected (green and blue) samples of our MSTO stars. The red and blue histograms are for the stars with $|Z| > 3$ kpc. *Right panel:* Same as in the left panel, but for the distributions of our adopted distance moduli. The red and blue histograms are for the stars with $[\text{Fe}/\text{H}] < -1.0$. The two panels indicate that the selection bias is very minimal when considering the stars with $|Z| > 3$ kpc or $[\text{Fe}/\text{H}] < -1.0$, for which halo stars are dominant.

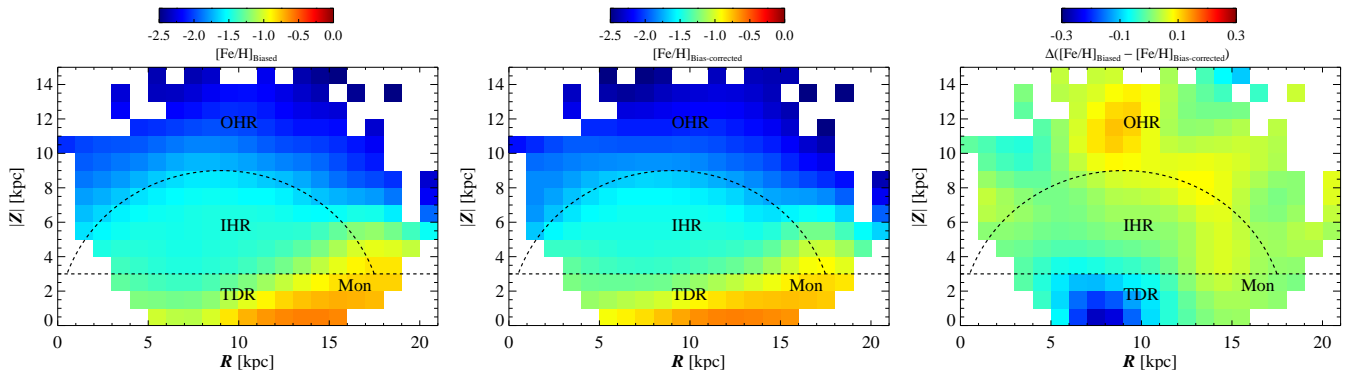


Figure 4. *Left panel:* Same as in Figure 1, but for $[\text{Fe}/\text{H}]$ of our original selection-biased sample. *Middle panel:* Same as in Figure 1, but for $[\text{Fe}/\text{H}]$ of the bias-corrected sample. The high metallicity region with $R > 15$ kpc and $|Z| < 5$ kpc indicates the Monoceros Stream (Newberg et al. 2002; Ivezić et al. 2008). It is marked with “Mon”. *Right panel:* Same as in Figure 1, but for the difference in $[\text{Fe}/\text{H}]$ between the biased and bias-corrected samples. Note that only small differences exist, with only regions near the disk approaching 0.3 dex.

stars selected for spectroscopic observation to the number of stars present in the direction of a given plug-plate with available photometry in each magnitude and color bin. We corrected for the selection bias of our MSTO stars by taking the inverse of the selection function for each object. We then cross-checked our estimation of the selection function for a subset of our sample with that derived by Mints & Hekker (2019), and confirmed good agreement.

After obtaining the selection function, we compared the metallicity distribution function (MDF) of the as-observed, and potentially biased sample (black histogram) with that (green histogram) of the bias-corrected sample, as shown in the left panel of Figure 3. In the figure, we see clearly that our sample has a relatively greater fraction of metal-poor stars for $[\text{Fe}/\text{H}] <$

-1.0 , and a smaller number of metal-rich stars for $[\text{Fe}/\text{H}] > -1.0$. However, if we restrict our sample of stars to $|Z| > 3$ kpc, for which the halo stars are dominant and in which we are most interested, the selection bias of our sample is minimal as can be seen by inspection of the blue and red histograms in the left panel of Figure 3.

We recognize as well that the selection bias that we want to remove is not only a function of $[\text{Fe}/\text{H}]$, but also possibly a function of distance and age. We investigated the possible distance bias, as shown in the right panel of Figure 3, which shows the distributions of the distance moduli (DM). The distance moduli were calculated based on our adopted distance derived by the SSPP. The black histogram represents the biased sample of our MSTO stars, while the green histogram applies to the unbiased sample. Comparison of the two histograms reveals that

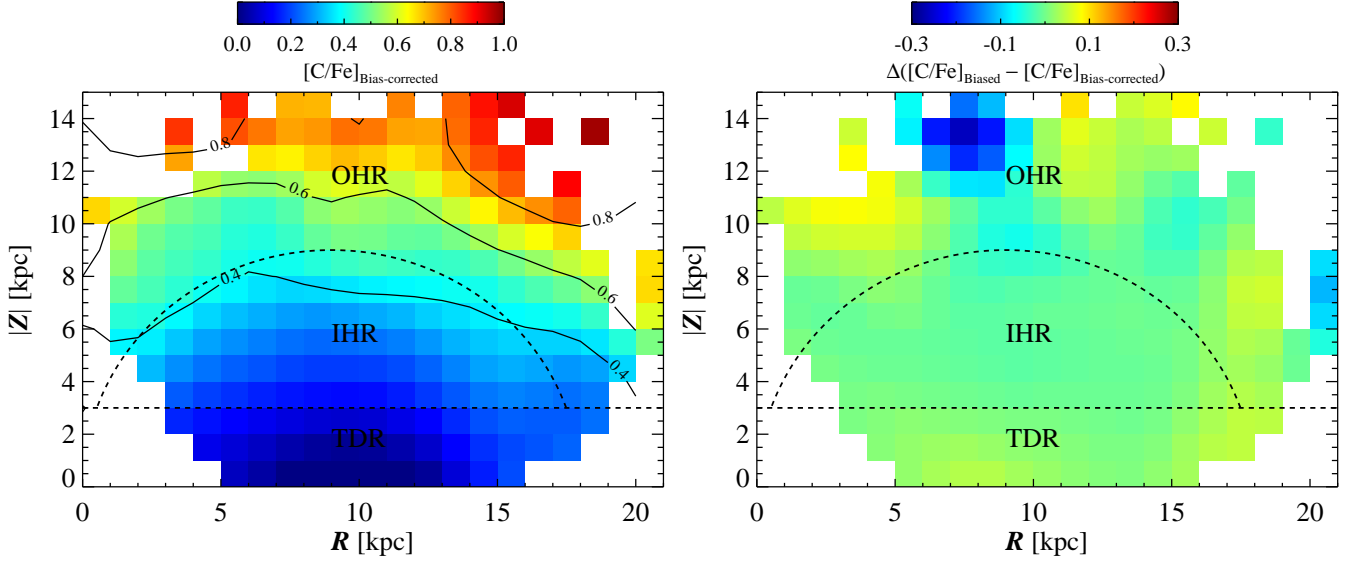


Figure 5. *Left panel:* Same as in Figure 1, but for the $[C/Fe]$ of the bias-corrected sample. *Right panel:* Same as in Figure 1, but for the difference in $[C/Fe]$ between the biased and bias-corrected samples.

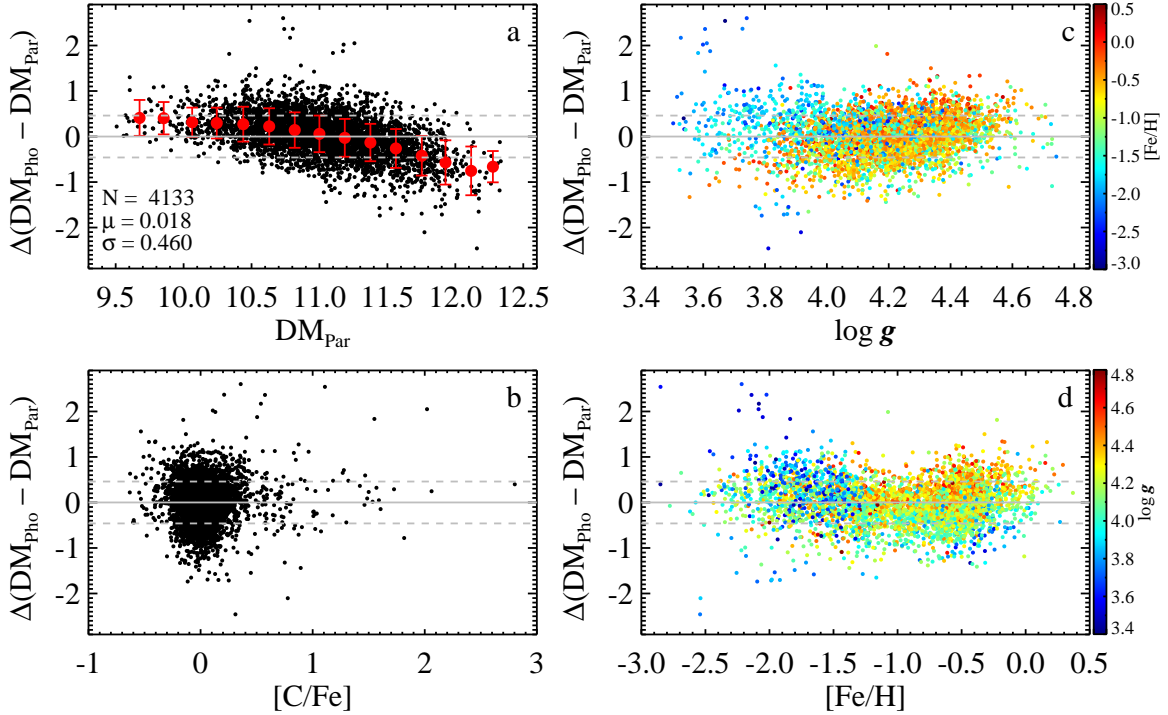


Figure 6. Residual plots of distance moduli between our photometric distance (DM_{pho}) and that (DM_{par}) from *Gaia* DR2, as a function of DM_{par} (panel a), $[C/Fe]$ (panel b), $\log g$ (panel c), and $[Fe/H]$ (panel d). We adjusted the *Gaia* parallax by -0.054 mas, and considered only stars that satisfy $\sigma_{\pi}/\pi < 0.1$ and $\sigma_{\pi} \leq 0.07$ mas, where π indicates the parallax. The total number of stars, the mean offset, and the standard deviation are listed in the left-bottom corner of panel a. The gray-dashed lines indicate the 1σ regions. In panel a, each red dot indicates the mean value of stars in a bin of 0.4 mag in the distance modulus, and each bin is overlapped with the next neighboring bin by 0.2 mag. The error bar is derived from resampling stars 100 times in each bin. In panels c and d, the color-coded dots indicate the scale of metallicity and surface gravity, respectively, as shown in the color bar on the right.

the distribution of the unbiased sample is slightly shifted to shorter distance. However, as in the case of the metallicity, by restriction of our sample to $[Fe/H] < -1.0$, which is dominated by halo stars, the distance bias arising from the target selection is clearly diminished, as can be seen from comparison of the red (biased) and blue (unbiased) histograms.

Concerning the age bias, since the stars in the halo

region ($|Z| < 15$ kpc) under question in this study have, on average, similar ages greater than 12 Gyr (Santucci et al. 2015; Carollo et al. 2016; Das et al. 2016), we can assume that the selection function has little dependence on stellar age, and would not affect our analysis.

We also investigated how the selection bias against the metal-rich stars is reflected in the metallicity map, where we want to delineate the Galactic halo region. Figure

4 compares the map of our original sample (left panel) with that of the bias-corrected (middle panel) samples. It appears that there is little difference between our sample map and unbiased maps. It is also very clear that the division line between the IHR and OHR (obtained by inspection of the carbonicity map of Figure 1) is well-established in both maps.

The right panel of Figure 4 quantitatively shows the difference between the left and the middle panel. According to the difference map, even though there are small deviations present, they are less than 0.1 dex over most of the map, except for the disk region (which is not of interest to this study), for which the discrepancy is as high as 0.3 dex.

As a further test, we identified the Galactic halo regions on the carbonicity map obtained after correcting for the target-selection bias, as shown in the left panel of Figure 5. Compared to Figure 1, even if the contour lines are slightly changed, we can tell that the boundary for the OHR established in the original carbonicity map is well-represented in the bias-corrected map. The right panel of Figure 5, which shows the difference between the selection-biased carbonicity map (Figure 1) and the unbiased carbonicity map (left panel of Figure 5), quantitatively underscores the minor impact of the target-selection bias, as it exhibits very small variations, of less than 0.1 dex in $[C/Fe]$, over most of the halo region.

One may naively think that the carbonicity map (Figure 1) might be predictable from the metallicity map (left panel of Figure 4), as apparently we can observe a well-behaved trend between $[C/Fe]$ and $[Fe/H]$. However, since the carbon enhancement varies with $[Fe/H]$ unpredictably, and the different stellar types and luminosity classes exhibit different levels of carbon enhancement (e.g., Rossi et al. 1999; Lee et al. 2013; Yong et al. 2013; Placco et al. 2014; Yoon et al. 2016), it is, in fact, not possible to predict the carbonicity map from the metallicity map. In addition, one can notice a less-smooth distribution of the carbonicity map than for the metallicity map, which would not be predicted from the metallicity map. We conclude that the carbonicity map enables us to better understand the nature of the Galactic halo, complimenting the metallicity map.

Summarizing, Figures 3, 4, and 5 suggest that the selection bias present in our MSTO sample does not significantly affect the metallicity and carbonicity distributions over the Galactic halo region under investigation, and might only be a concern if one wants to derive the exact shape of the sample MDF. This is primarily due to the fact that the photometric target selection quickly loses metallicity sensitivity below $[Fe/H] = -2.0$. Our examination of large swaths of sky in performing our analysis also mitigates the potential impact in any given direction. Thus, in the following analysis and discussion, we employ the original MSTO halo stars, without applying corrections for the selection bias unless otherwise specifically mentioned.

3.2. Distance Errors

In order to check on the accuracy of our derived distance scale, we matched our MSTO sample with stellar sources in *Gaia* DR2, and selected stars with high-precision parallaxes, by applying $\sigma_\pi/\pi < 0.1$ and $\sigma_\pi < 0.07$ mas, as suggested by Schönrich et al. (2019), where π

is the parallax and σ_π is the uncertainty. After adjusting for the known zero-point offset of -0.054 mas (Schönrich et al. 2019; Graczyk et al. 2019), we compared our derived distances with the *Gaia* DR2 distances. Figure 6 shows the differences in the distance moduli between our photometric distance (DM_{pho}) and that of *Gaia* DR2 (DM_{par}), as a function of DM_{par} (panel a), $[C/Fe]$ (panel b), $\log g$ (panel c), and $[Fe/H]$ (panel d). The total number of stars, the mean offset, and the standard deviation are listed in the left-bottom corner of panel a. The gray-dashed lines indicate the 1σ regions. In panel a, each red dot represents a mean value of stars in a bin of 0.4 mag in the distance modulus, and each bin is overlapped with the next neighboring bin by 0.2 mag. The error bar is derived from resampling stars 100 times in each bin. In panels c and d, the color-coded dots indicate the scale of metallicity and surface gravity, respectively, as shown in the color bar on the right.

Inspection of panel a of the figure reveals that, even though there is a tendency such that our distance estimate is slightly lower for the most remote stars and slightly higher for closer stars, the overall systematic offset in the distance is very small. We note that the distance moduli of our MSTO stars mostly agree very well with those having *Gaia* DR2 parallaxes, and are within 2σ for more than 95% of the stars considered. Moreover, it is noteworthy that the trend (red dots) of the mean offset with DM_{par} is within the 1σ region, after taking into account the error bar of each red dot. Additionally, in panels b, c, and d of Figure 6, we do not see evidence for any trends between our spectroscopic distance moduli and the *Gaia* DR2 moduli over $[C/Fe]$, $\log g$, and $[Fe/H]$, respectively, indicating that there exists no significant systematic errors in our derived distance scale due to the presence of strong carbon bands or incorrect assignment of the luminosity class. We also do not find any complex trends among the parameters (panels c and d). These tests indicate the robustness of our distance estimates.

4. CHEMICAL AND KINEMATIC SIGNATURES OF DISTINCT POPULATIONS IN THE GALACTIC HALO

In this section, we seek to identify differences in stellar populations in the Galactic halo by searching for distinguishing trends in their chemistry and kinematics.

4.1. Chemical Signatures

We first examine the carbonicity and metallicity distributions in the X - Y plane in different regions of $|Z|$. Figure 7 exhibits the metallicity maps for our MSTO sample in the X and Y plane for the regions of $|Z| \leq 3$ kpc (left panel), $3 < |Z| \leq 9$ kpc (middle panel), and $|Z| > 9$ kpc (right panel). These regions approximately correspond to the TDR, IHR, and OHR, respectively. In this plane, our Sun is located at $(X, Y) = (8, 0)$ kpc. Each bin with a size of 1×1 kpc contains at least three stars, and represents a median value of $[C/Fe]$, with the color scale shown in the color bar. The general trend noted in the figure is that the overall metallicity distribution decreases with increasing distance from the Galactic plane. It is interesting to note in the left panel of Figure 7 the unexpected positive metallicity gradient with the distance from the Galactic center at a given Y . This may arise from the presence of the Monoceros Stream at $X > 11$ kpc. In the

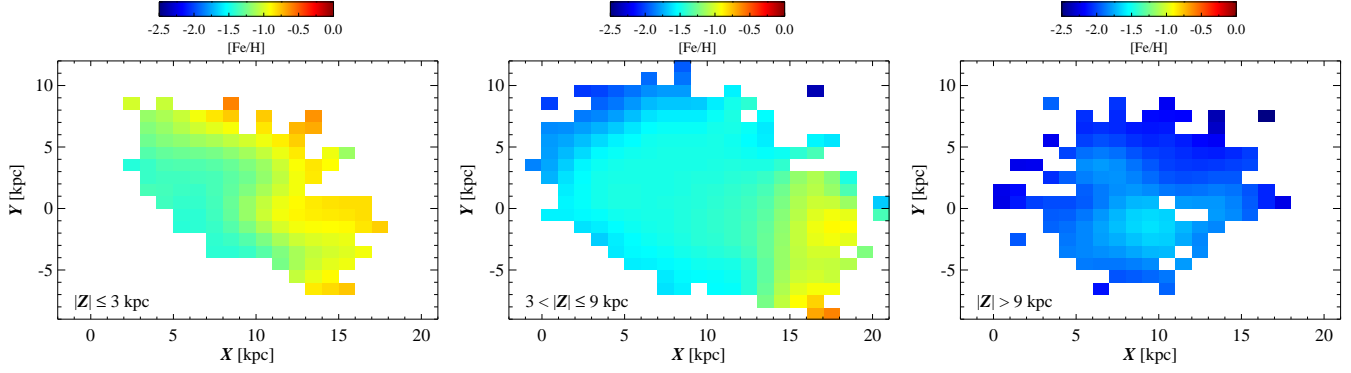


Figure 7. Metallicity maps for our MSTO sample in the X and Y plane, in the range of $|Z| \leq 3$ kpc (left panel), $3 < |Z| \leq 9$ kpc (middle panel), and $|Z| > 9$ kpc (right panel), which approximately correspond to the TDR, IHR, and OHR, respectively. In this plane, our Sun is located at $(X, Y) = (8, 0)$ kpc. The bin size is 1×1 kpc. Each pixel contains at least three stars and represents a median value of $[\text{Fe}/\text{H}]$, with the color scale shown in the color bar.

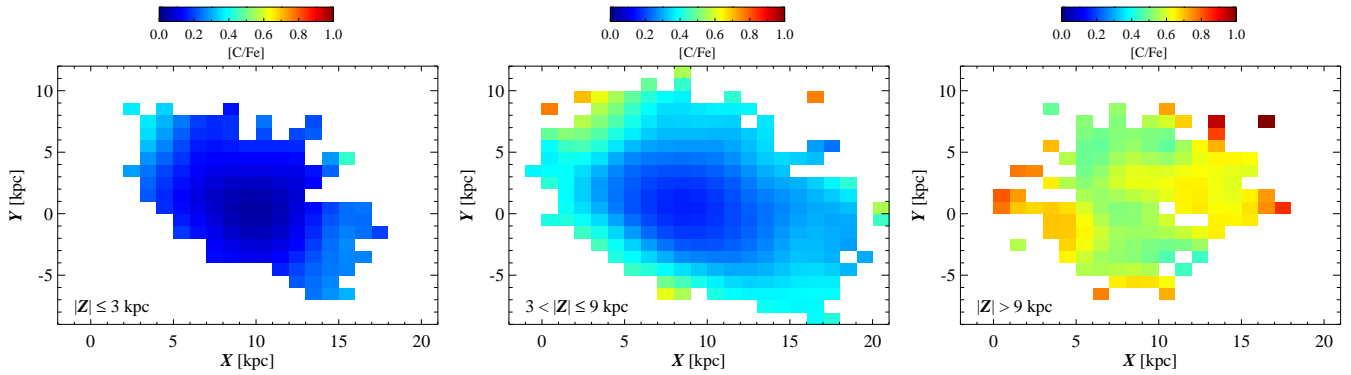


Figure 8. Same as in Figure 7, but for $[\text{C}/\text{Fe}]$.

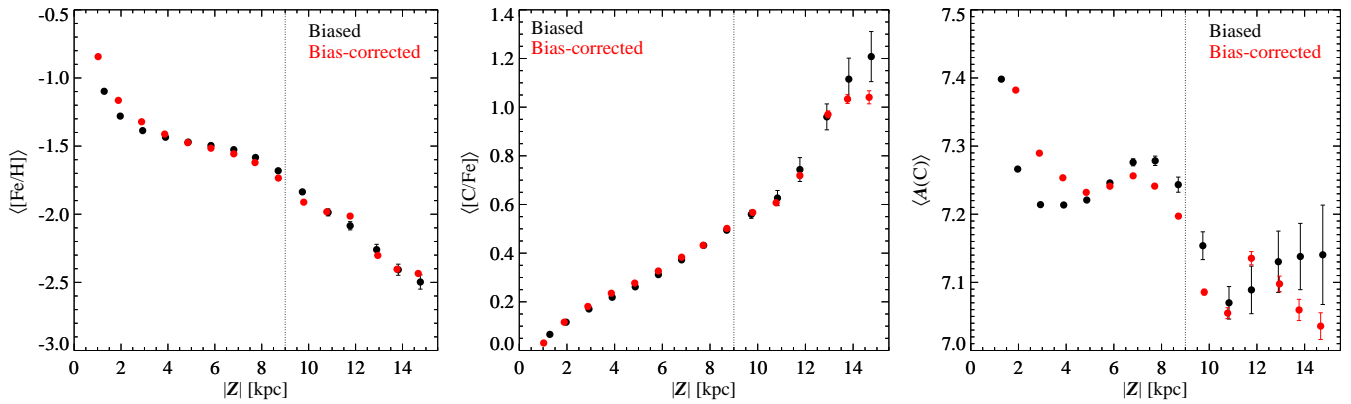


Figure 9. Distributions of mean values of $[\text{Fe}/\text{H}]$ (left panel), $[\text{C}/\text{Fe}]$ (middle panel), and $A(\text{C})$ (right panel), as a function of $|Z|$. Each dot represents the mean value for stars within a bin of 2 kpc, and each bin is overlapped with the next neighboring bin by 1 kpc. The error is the standard deviation derived by resampling stars 100 times in each bin. The red dots are derived from the sample corrected for the selection bias. The left panel exhibits a slow decrease of $\langle [\text{Fe}/\text{H}] \rangle$ between $|Z| = 3$ and 8 kpc, and a rather dramatic decrease of $[\text{Fe}/\text{H}]$ beyond $|Z| = 8$ kpc. The bias-corrected sample also shows very similar trend. The middle panel shows a steady increase of $\langle [\text{C}/\text{Fe}] \rangle$ up to $|Z| = 11$ kpc, and a rapid increase beyond $|Z| = 11$ kpc, even though the bias-corrected sample exhibits a somewhat lower increase. In the right panel, the mean value of $\langle A(\text{C}) \rangle$ gradually increases between $|Z| = 3$ kpc and 8 kpc, then abruptly drops up to $|Z| = 11$ kpc, and exhibits a constant, lower value of $A(\text{C})$ for both the biased and bias-corrected samples. The vertical dotted line at $|Z| = 9$ kpc indicates the highest $|Z|$ point in the region that separates the IHR from the OHR in Figure 1.

middle panel, we can also see the higher metallicity region at $X > 14$ kpc, likely associated with the Monoceros Stream as well.

Figure 8 shows the carbonicity maps at different heights above the Galactic plane. The layout is the same as in Figure 7. In these plots, as expected, we notice the higher $[\text{C}/\text{Fe}]$ at higher $|Z|$. Particularly, the two groups with relatively larger enhancement of carbon in the right

panel imply the presence of substructures in the OHR in our sample.

For a more quantitative analysis, we present in Figure 9 profiles of the mean values of $[\text{Fe}/\text{H}]$ (left panel), $[\text{C}/\text{Fe}]$ (middle panel), and $A(\text{C})$ (right panel), as a function of $|Z|$. Each dot represents an average value for stars within a bin of 2 kpc width, overlapped with the next neighboring bin by 1 kpc. The error bars are obtained

by bootstrapping the sample 100 times in each bin. The vertical dotted lines indicate the the radius of the IHR determined from the carbonicity map shown in Figure 1. Similarly, the red dots are derived from the sample corrected for target-selection bias.

The left panel of Figure 9 reveals three distinct features in the metallicity profile – a rapid decrease in $\langle[\text{Fe}/\text{H}]\rangle$ up to $|Z| = 3$ kpc, a mild decline between $|Z| = 3$ and 8 kpc, and a continuous decrease beyond $|Z| = 8$ kpc. These transition regions in the $[\text{Fe}/\text{H}]$ profile correspond well with each Galactic region assigned in the carbonicity map. We note that the bias-corrected sample also exhibits a very similar trend.

We derived a metallicity gradient of -0.172 ± 0.043 dex $^{-1}$ kpc $^{-1}$ over $|Z| < 3.0$ kpc (the location of the TDR), -0.037 ± 0.004 dex $^{-1}$ kpc $^{-1}$ over $3 \leq |Z| < 8$ kpc, which roughly corresponds to the IHR, and -0.136 ± 0.003 dex $^{-1}$ kpc $^{-1}$ over $|Z| \geq 8$ kpc, which we associate with the OHR. The mild metallicity gradient in the IHR suggests that stars in the IHR experienced similar chemical-enrichment histories, whereas the relatively steeper metallicity gradient in the OHR suggests a more complex star-formation history, possibly involving the accretion of multiple mini-halos, which may have contributed lower metallicity stars to the OHR.

Our derived metallicity gradient for the OHR is rather steeper than the results from the simulations of the MW-like galaxies. For example, Tissera et al. (2014) obtain, based on six stellar halos from Aquarius simulation project (Scannapieco et al. 2009), a metallicity gradient between -0.002 and -0.008 dex $^{-1}$ kpc $^{-1}$. However, the halo region they consider is $r > 20$ kpc, which is much more distant than our OHR.

The metallicity gradient of our sample in the OHR is also larger than that (~ -0.001 dex $^{-1}$ kpc $^{-1}$) of Das & Binney (2016), derived from an extended distribution function fit to SEGUE K giants with $[\text{Fe}/\text{H}] < -1.4$. Their K giants are also mostly located at distance greater than 10 kpc from the Galactic center. Consequently, as their stellar species and distance coverage are different from our sample, it is difficult to directly compare their result and ours. Nonetheless, if we only consider the stars with $[\text{Fe}/\text{H}] < -1.4$ and $|Z| > 8$ kpc, we obtain slightly smaller gradient of ~ -0.1 dex $^{-1}$ kpc $^{-1}$.

The above behavior stands in contrast to that observed in the the middle panel of the figure, the average carbonicity profile. The $\langle[\text{C}/\text{Fe}]\rangle$ value steadily increases up to $|Z| = 11$ kpc, with a more rapid increase beyond $|Z| = 11$ kpc, which may be a signature of the existence of chemical substructure in the OHR. Even though the increasing trend at higher $|Z|$ is somewhat weak, we notice the similar trend from the bias-corrected sample (red dots).

Differences in the nature of the stellar populations between the IHR and OHR become more clear in the distribution of $\langle A(\text{C}) \rangle$ in the right panel of Figure 9. The mean value of $A(\text{C})$ drops rapidly over $|Z| < 3.0$ kpc (the TDR), then slightly increases between $|Z| = 3$ kpc and 8 kpc (the IHR), and then abruptly drops up to $|Z| > 11$ kpc (the OHR), and remains at a lower value of $A(\text{C})$ for both the biased and bias-corrected samples. These trends suggest that the progenitors that contributed to the formation of IHR differ from those that contributed

to the OHR, a clear indication of the duality (at least) of the Galactic halo.

4.2. Kinematic Signatures

As the kinematics associated with different stellar populations in the halo can provide valuable clues to its assembly history, we now examine the nature of the velocity structure associated with the components identified in the carbonicity map, beginning with the spatial distribution of the rotational velocity and the mean velocity and velocity dispersion profiles, followed by consideration of the differences revealed in their velocity ellipsoids and anisotropies.

4.2.1. Velocity Structure

We first investigated the distribution of rotational velocities for our sample in the X - Y plane in different bins of $|Z|$, as shown in Figure 10. The layout of the figure is the same as in Figure 7. Generally, we observe a more retrograde motion at larger distances from the Galactic plane. One interesting aspect is a small, patchy area with relatively stronger counter-rotation in the IHR (middle panel), indicative of substructures in velocity space.

Figure 11 shows the profiles of mean velocities (top panel) and dispersions (bottom panel) in spherical coordinates, as a function of $|Z|$. The black dots correspond to V_r , while the red triangles represent V_θ , and the green squares indicate V_ϕ . Each symbol represents an average value in a bin size of 2 kpc in $|Z|$, with each bin overlapped with the next neighboring bin by 1 kpc. The error bar is the bootstrap estimate of the standard deviation based on 100 realizations. The vertical dotted line marks the highest point in the region that separates the IHR from the OHR.

Inspection of the top panel of Figure 11 reveals that the rotation velocity indicated by the green squares rapidly decreases from ~ 100 km s $^{-1}$ at $|Z| = 1$ kpc to almost zero at $|Z| = 5$ kpc, then continues to decline, exhibiting a small retrograde motion. Above $|Z| = 9$ kpc, stars show significant retrograde motions. In contrast, the other two velocity components (V_r and V_θ) do not vary around $\langle V \rangle = 0$ km s $^{-1}$ over the vertical distance considered. The V_ϕ behavior in the region of the TDR is expected from an overlap between stars belonging to the metal-weak thick disk and of the IHP over $1 < |Z| < 5$ kpc. Beyond 5 kpc from the plane, the observed behavior of V_ϕ can be accounted for by the gradual transition from the dominant contribution by stars of the IHP to the OHP; even though there are fewer stars in our MSTO sample far from the plane, they display significantly different V_ϕ .

Similar distinct behaviors can be also found from inspection of the bottom panel of Figure 11, which presents the velocity dispersion profiles. The dispersion in V_ϕ does not change dramatically between 90 and 110 km s $^{-1}$ over $|Z| < 9$ kpc, while it increases to between 130 and 160 km s $^{-1}$ above $|Z| = 9$ kpc. The dispersion of V_r increases with $|Z|$ distance in the TDR, does not change much in the IHR, then declines to ~ 90 km s $^{-1}$ in the OHR. The dispersion of V_θ generally exhibits a continuously increasing trend. In the figure, we note that the dispersion of V_r is much larger than either V_θ and V_ϕ in the IHR (i.e., the velocity ellipsoid of the IHR is dominated by large radial motions, as shown by many previous studies), but

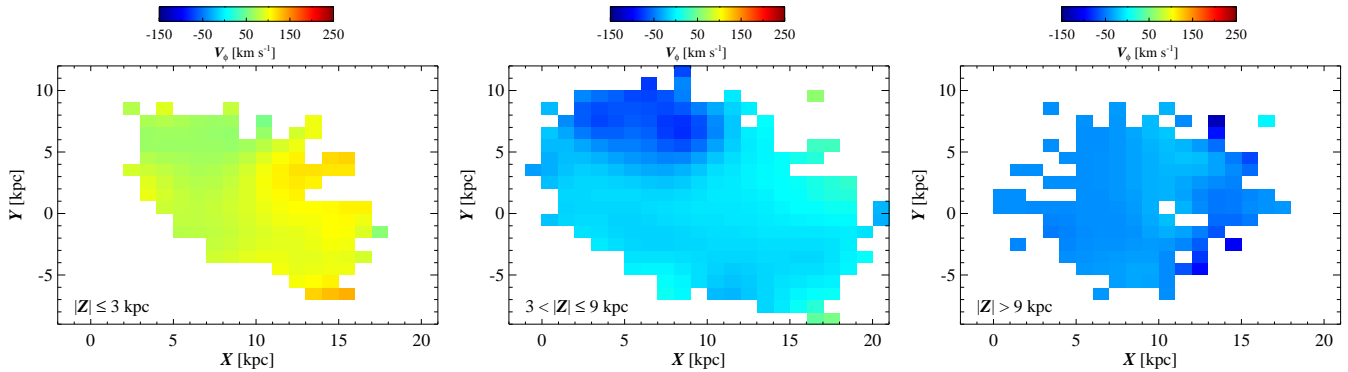


Figure 10. Same as in Figure 7, but for V_ϕ .

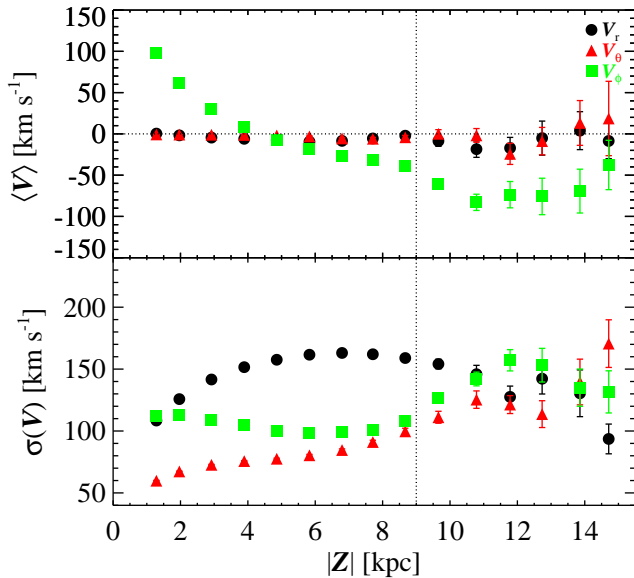


Figure 11. Trends of mean velocities (top panel) of V_r (black symbols), V_θ (red symbols), and V_ϕ (green symbols) and their dispersions (bottom panel) in spherical coordinates, as a function of $|Z|$. Each dot covers a bin size of 2 kpc, and each bin is overlapped with the next neighboring bin by 1 kpc. The error bar is the standard deviation of 100 realizations obtained by bootstrapping. The vertical dotted line at 9 kpc indicates the highest point in the region that separates the IHR from the OHR in Figure 1, whereas the horizontal dotted line provides a reference at 0 km s^{-1} . In the top panel, the mean rotational velocity (green symbols) steeply decreases in the disk region ($|Z| < 4$ kpc), declines very slowly up to 9 kpc, and then decreases again beyond $|Z| = 9$ kpc, becoming retrograde. The other two velocity components exhibit almost zero velocity throughout the region considered. Interestingly, we note that the dispersion in V_r crosses over the V_θ and V_ϕ dispersions at about 11 kpc, consistent with a transition from the IHP to the OHP in our sample.

decreases in the OHR, again indicating contrasting behavior relative to the IHR.

Taken as a whole, Figure 11 indicates that the transition regions identified in the trends of the mean velocity and velocity dispersion correspond (at least qualitatively) to the differences found in the metallicity and carbonicity profiles shown in Figure 9. This strongly suggests that differences in the stellar populations of the halo are revealed by our MSTO stellar sample.

We now consider the distribution of the median and dispersion of the velocity components in the spatial domain. Figure 12 presents maps of the medians in V_r (left panel), V_θ (middle panel), and V_ϕ (right panel) compo-

nents in the $|Z|$ and R plane. Each bin has a dimension of 1×1 kpc and has at least three stars. The dashed lines are the boundaries for the Galactic components defined in Figure 1. Note that, owing to the absence of the proper motions of some stars, the shape of the map is slightly different from Figure 1. In the map, due to the small number of stars in some bins, we considered the median instead of the mean for a more robust estimate.

The figure indicates that the medians of V_r and V_θ in the IHR are mostly between -10 km s^{-1} and $+10 \text{ km s}^{-1}$, and there exists no radial or vertical gradient in V_r and V_θ , as already seen in Figure 11. We can also notice almost no rotation (V_ϕ) of the IHR, but there is weak vertical and radial gradient in V_ϕ . We can see the Monoceros Stream (Newberg et al. 2002; Ivezić et al. 2008), with a high rotation velocity, as well.

By contrast, in the OHR we see several clumpy structures for V_r and V_θ , as well as relatively milder retrograde and stronger counter rotation in some regions. In these maps, we notice that the boundary defined in Figure 1 between the IHR and OHR corresponds well with structures in the three velocity components, which suggests that the chemical division of the stellar populations can identify distinct kinematic properties as well.

Figure 13 shows maps of the velocity dispersions. The layout of the figure is the same as in Figure 12. Inspection of this figure reveals that the dispersion of V_r becomes higher towards the bulge and Galactic North Pole. At a given $|Z|$, it exhibits a clear radial gradient, while the V_θ dispersion exhibits a moderate vertical gradient. The obvious offset of the high radial dispersion population in the direction toward the Galactic center supports the identification by numerous recent studies of the “Gaia Sausage” (Belokurov et al. 2018) or Gaia-Enceladus (Helmi et al. 2018) structure. There exists no strong dispersion gradient in V_ϕ within the IHR, although the dispersion increases in the OHR. Generally, the IHR-OHR boundary is well-delineated in the dispersion maps of V_θ and V_ϕ . The clumpy structures in the OHR seen in Figure 12 and the relatively higher velocity dispersions shown in Figure 13 strongly suggest that the stars in the IHR have experienced different assembly histories from those in the OHR.

The derived mean velocities and dispersions of each velocity component (in both spherical and cylindrical systems) for each Galactic region are listed in Table 1, along with their bootstrapped errors based on 100 resamples. We first consider the detailed behavior of the rotational component V_ϕ (in the cylindrical system, which is the

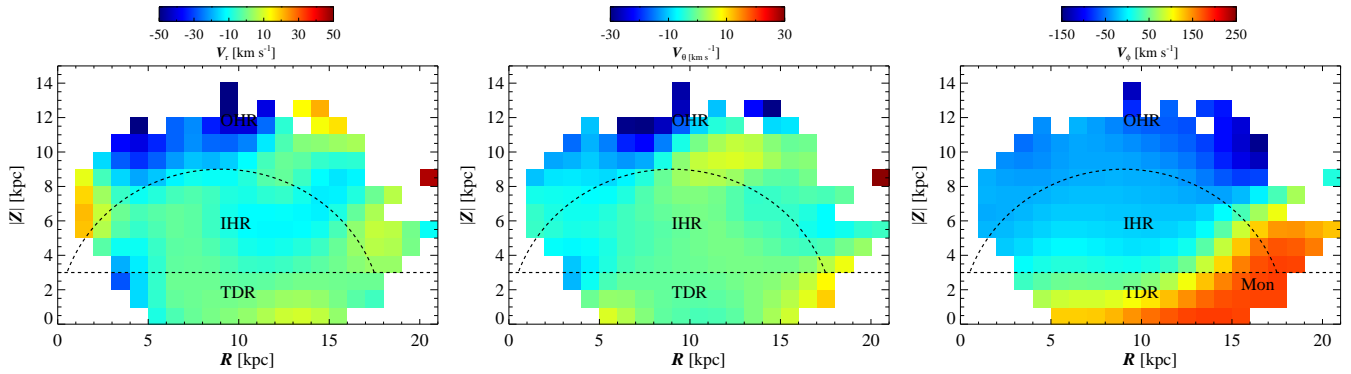


Figure 12. Maps of the medians of V_r (left), V_θ (middle), and V_ϕ (right) components in the $|Z|$ and R plane. Due to the small number of stars in some bins, we considered the median instead of the mean. Each bin has a size of 1×1 kpc and at least three stars. The dashed lines are the boundaries for the Galactic components defined in Figure 1. We note that the IHR and OHR are well-distinguished in the three velocity components. “Mon” in the right panel indicates the Monoceros Stream.

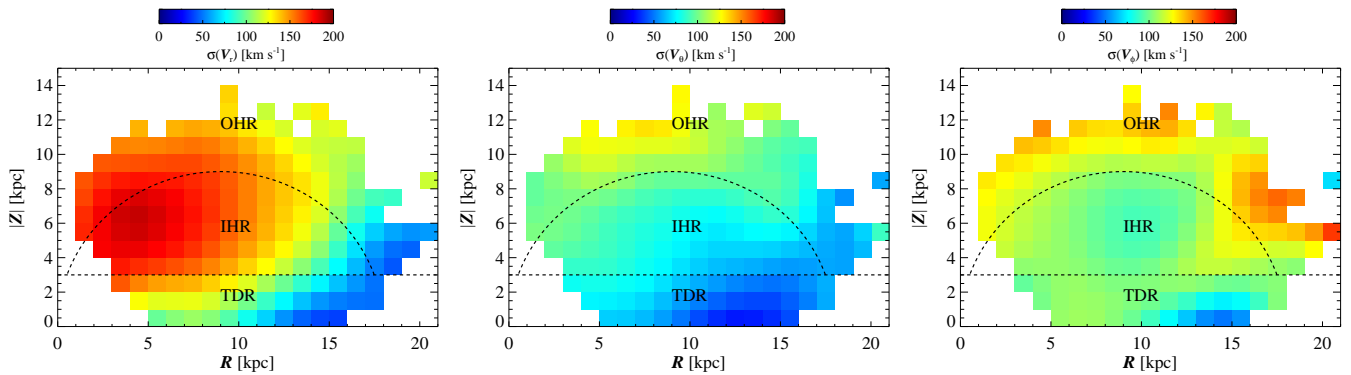


Figure 13. Same as in Figure 12, but for the velocity dispersions of the three components.

Table 1
Kinematic Properties in Spherical and Cylindrical Coordinates for each Galactic Region

Spherical							
Region	N_{tot}	V_r	V_θ	V_ϕ	σ_{V_r}	σ_{V_θ}	σ_{V_ϕ}
		(km s^{-1})	(km s^{-1})	(km s^{-1})	(km s^{-1})	(km s^{-1})	(km s^{-1})
TDR	55769	-1.1 ± 0.5	-0.9 ± 0.3	75.7 ± 0.5	119.8 ± 0.5	64.3 ± 0.4	114.6 ± 0.3
IHR	44546	-7.0 ± 0.8	-2.1 ± 0.3	-2.6 ± 0.5	155.6 ± 0.5	78.1 ± 0.3	102.7 ± 0.4
OHR	1169	-5.8 ± 4.5	-6.7 ± 3.1	-49.3 ± 3.7	152.6 ± 2.6	108.8 ± 2.9	130.0 ± 2.8
Cylindrical							
Region	N_{tot}	V_R	V_Φ	V_Z	σ_{V_R}	σ_{V_Φ}	σ_{V_Z}
		(km s^{-1})	(km s^{-1})	(km s^{-1})	(km s^{-1})	(km s^{-1})	(km s^{-1})
TDR	55769	-1.3 ± 0.5	75.7 ± 0.5	0.7 ± 0.3	117.5 ± 0.4	114.6 ± 0.3	68.4 ± 0.3
IHR	44546	-8.6 ± 0.7	-2.6 ± 0.5	-0.7 ± 0.5	144.9 ± 0.4	102.7 ± 0.4	96.5 ± 0.4
OHR	1169	-12.7 ± 4.5	-49.3 ± 3.7	-3.1 ± 4.0	140.7 ± 2.6	130.0 ± 2.8	123.4 ± 2.4

Note. — N_{tot} is the total number of stars in each Galactic region. The listed uncertainties are derived from 100 bootstrapped resamples. By coordinate configuration, V_ϕ is equal to V_Φ . β is the anisotropy parameter calculated by Equation (1).

same as V_ϕ in the spherical system). We obtained on average $\langle V_\Phi \rangle = -2.6 \pm 0.5 \text{ km s}^{-1}$ for the IHR and $-49.3 \pm 3.7 \text{ km s}^{-1}$ for the OHR, clear evidence for its retrograde motion.

Since it is possible for disk stars to reach distances from the plane (for example, due to disk heating) that are sufficiently large to be confused with halo stars, we have checked how potential contamination from disk stars could affect the derived rotation velocities by restricting our MSTO sample to stars with $[\text{Fe}/\text{H}] < -1.0$, as most of disk stars have $[\text{Fe}/\text{H}] > -1.0$. After making this restriction, we obtained $\langle V_\Phi \rangle = -17.5 \pm 0.5 \text{ km s}^{-1}$ for

the stars in the IHR, and $\langle V_\Phi \rangle = -60.5 \pm 3.9 \text{ km s}^{-1}$ for the stars in the OHR, indicating a larger retrograde motion for each halo. However, as we want to study the *in situ* halo, we consider all of our MSTO stars in our analysis, without removing the possible disk stars.

4.2.2. Comparisons with Other Studies

Our average value of V_Φ for the IHR stars is not far from that ($7 \pm 4 \text{ km s}^{-1}$) derived by Carollo et al. (2010), while our derived $\langle V_\Phi \rangle$ of -49 km s^{-1} suggests that the counter-rotating signal is slightly weaker than that ($-80 \pm 13 \text{ km s}^{-1}$) reported by Carollo et al. (2010), even

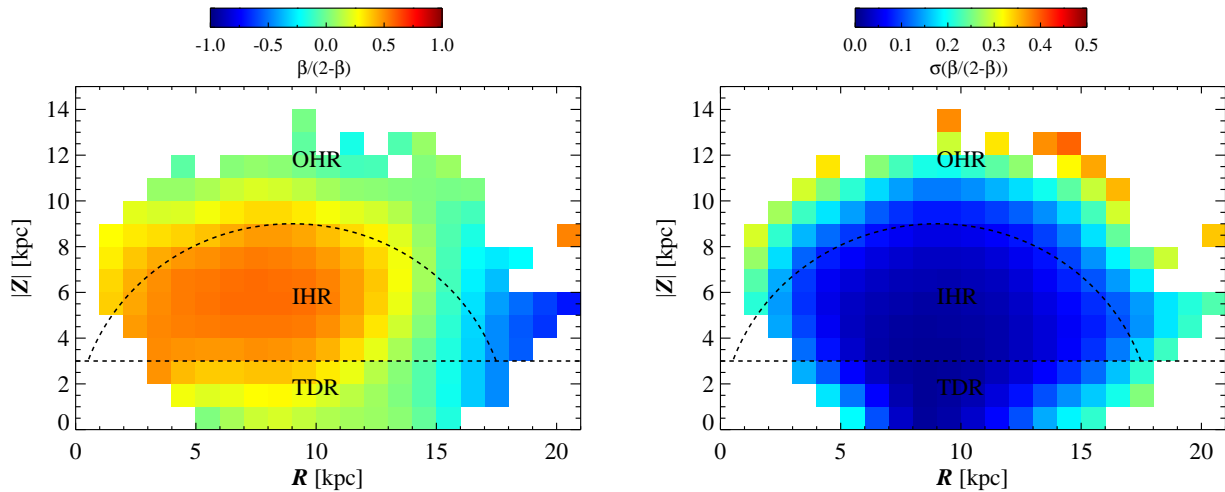


Figure 14. Same as in Figure 12, but for the rescaled anisotropy parameter, $\beta^* = \beta/(2 - \beta)$ (left panel) and its scatter (right panel), based on 100 samples generated from a Monte Carlo simulation.

taking the errors into account. We found a dispersion for V_ϕ of 103 and 130 km s⁻¹ for the IHR and OHR, respectively, compared to 95 ± 2 and 165 ± 9 km s⁻¹ derived by Carollo et al.

The above discrepancies may arise in part from the fact that Carollo et al. (2010) employed a local sample of stars, with distances less than 4 kpc from the Sun, and separated the various halo populations based on the kinematic information itself, while our separation is purely based on the spatial distribution of [C/Fe]. Thus, the two methods are describing two different aspects of the data – one a population-based method, and the other an in-situ method (wherein overlapping inner- and outer-halo populations can contribute, in particular for the IHR).

Comparing with the other two cylindrical velocity components for the IHP and OHP given in Table 5 of Carollo et al. (2010), our value of $V_R = -8.6$ km s⁻¹ for the IHR is slightly lower than their value of 3 km s⁻¹ for the IHP, while our value of -12.7 km s⁻¹ for the OHR does not differ much from their value of -9 km s⁻¹. Our derived dispersions for V_R are 145 and 141 km s⁻¹ for the IHR and OHR, respectively, while theirs are 150 and 159 km s⁻¹ for the IHP and OHP, respectively. For the V_Z component, we derived average values of -1 (97) and -3 (123) km s⁻¹ (where the number listed in parentheses is the dispersion), compared to their values of 3 (85) and 2 (116) km s⁻¹ for the IHP and OHP, respectively. Once again, the small differences in these quantities are likely due to their different definitions and techniques for separation of the sample stars.

We now consider the results obtained by a number of other recent studies. Kafle et al. (2017) also use SDSS MSTO stars to investigate the kinematic properties of stars in the region $r \leq 15$ kpc from the Galactic center and $|Z| > 4$ kpc from the Galactic plane. Interestingly, they find for the mean and dispersion of the rotation velocity component values of -16 (72) km s⁻¹ for a metal-rich group ($[\text{Fe}/\text{H}] > -1.4$) and 26 (82) km s⁻¹ for a metal-poor group ($[\text{Fe}/\text{H}] < -1.4$). Apparently, for the OHR our mean value has opposite sign to theirs, while our derived dispersion is higher than theirs. If we consider our sample separated by their criteria, we obtained $\langle V_\phi \rangle = 2$ (87) km s⁻¹ for the metal-rich component and

-31 (102) km s⁻¹ for the metal-poor component.

Deason et al. (2017) make use of the SDSS data and proper motions from the first data release of *Gaia* (Gaia Collaboration et al. 2016) to derive $\langle V_\phi \rangle = 12$ km s⁻¹ from RR Lyrae, 6.0 km s⁻¹ from blue horizontal branch (BHB) stars, and 23 km s⁻¹ from K giants. These stars reach up to 50 kpc from the Galactic center and do not include stars with $|Z| < 4$ kpc, which correspond to the disk populations. Although they find that metal-poor population ($[\text{Fe}/\text{H}] < -1.5$) exhibits a slightly lower rotation velocity than the metal-rich population for all three stellar types, their metal-poor population does not show retrograde motion, contrary to our metal-poor counterpart ($[\text{Fe}/\text{H}] < -1.4$), which has $\langle V_\phi \rangle = -31$ km s⁻¹.

On the other hand, Belokurov et al. (2018) analyze MS stars in the SDSS to compute $\langle V_\phi \rangle = 20 - 30$ km s⁻¹ for stars with $-1.0 < [\text{Fe}/\text{H}] < -1.7$ and $1 < |Z| < 9$ kpc. They also find that the metal-poor stars with $[\text{Fe}/\text{H}] < -1.7$ exhibit various values of $\langle V_\phi \rangle$ from 15 to 50 km s⁻¹, depending on the range of $|Z|$ investigated. In contrast, we found between -20 and 20 km s⁻¹ for the metal-rich component, and between -46 and -4 km s⁻¹ for the metal-poor component in the three regions ($1 < |Z| < 3$ kpc, $3 < |Z| < 5$ kpc, and $5 < |Z| < 9$ kpc) of $|Z|$ they considered.

Summing up the aforementioned studies, although we found that there does exist some correlation between the stellar rotation velocity and metallicity, the reviewed literature does not report a significant counter-rotating signature.

4.2.3. Orbital Properties

We now examine the distribution of stellar orbits in the halo populations quantified by the velocity anisotropy parameter (Binney & Tremaine 2008), given by

$$\beta = 1 - \frac{\sigma_\theta^2 + \sigma_\phi^2}{2\sigma_r^2} \quad (1)$$

where σ_r^2 , σ_θ^2 , and σ_ϕ^2 are the velocity dispersions in the spherical coordinate system. A value of $\beta = 0$ means that the two tangential components are equal to the radial component, suggesting the distribution of stellar orbits

is isotropic. When $\beta > 0$, the radial component is larger than the tangential components, corresponding to more radially elongated stellar orbits. On the other hand, values of $\beta < 0$ indicates a tangentially biased distribution of the stellar orbits.

Because the anisotropy parameter has a negatively skewed distribution, it is often rescaled by $\beta^* = \beta/(2 - \beta)$, so that the value of β^* has the range from -1 to 1 when investigating the overall description of orbital distributions. In the rescaled β^* case, the interpretation of a stellar system is the same as for β , such that if $\beta^* = 0$, a stellar system is isotropic, while for cases of $\beta^* < 0$ and $\beta^* > 0$, the system is tangentially and radially biased, respectively.

The left panel of Figure 14 is a map of the rescaled anisotropy parameter, $\beta^* = \beta/(2 - \beta)$, constructed in a similar manner as Figure 12. Inspection of the figure clearly shows the radially biased orbits of the stars in the IHR, while the stellar orbits in the OHR become more isotropic. It is also interesting to note that the stars in the region with $R > 15$ kpc and $|Z| < 6$ kpc have tangentially biased orbits. This is partly due to the presence of the Monoceros stellar stream (Newberg et al. 2002; Ivezić et al. 2008), which is included in the region.

Quantitatively, we obtained $\beta = 0.656$ and 0.383 for the IHR and OHR, respectively, as listed in the last column of Table 1, implying more spherical distribution of stellar orbits in the OHR. Our derived value of $\beta = 0.656$ for the IHR is mostly in good agreement with other studies. For example, previous studies of sub-dwarfs and MS stars from SDSS report $\beta \sim 0.68$ for the local halo, consistent with a radially biased distribution (Smith et al. 2009; Bond et al. 2010). Kafle et al. (2012) derive $\beta \sim 0.5$ from BHB stars observed by SDSS/SEGUE, covering the region $r = 9 - 12$ kpc from the Galactic center, which corresponds to our IHR. King et al. (2015) use a sample of stars observed with the MMT along with F-type and BHB stars from SDSS to derive the anisotropy parameter based on radial velocities alone. They find $\beta = 0.15 - 0.54$ in the range $r = 9 - 12$ kpc. Kafle et al. (2017) also obtain a value of 0.58 for metal-rich ($[\text{Fe}/\text{H}] > -1.4$) MSTO stars with $|Z| > 4$ kpc and $r \leq 15$ kpc from radial velocities alone. On the other hand, using SDSS-*Gaia* proper motions, Belokurov et al. (2018) report a higher value of $\beta \sim 0.9$ for MS stars with $[\text{Fe}/\text{H}] > -1.7$, located within ~ 10 kpc of the Sun, which differs from our value even though our IHR region covers a similar spatial and metallicity range. Nonetheless, the consensus from all of these studies is that there exists a radially biased velocity ellipsoid for the local/inner halo.

There is no such general consensus on the more distant outer halo, however. Our derived value of $\beta = 0.383$ for the OHR is between the values reported by previous studies that probe similar halo regions and metallicity ranges. For instance, Kafle et al. (2017) obtain $\beta = 0.62$ for metal-poor stars ($[\text{Fe}/\text{H}] < -1.4$) in the region of $|Z| > 4$ kpc and $11 < r \leq 15$ kpc. One possible cause of the difference is that they use only stellar radial velocities to calculate the velocity components in the spherical coordinates. Belokurov et al. (2018), however, report a similar range of $\beta = 0.2 - 0.4$ to our OHR value for metal-poor MS stars with $[\text{Fe}/\text{H}] < -1.7$. Interestingly, Kafle et al. (2012) suggest negative values of β from BHB stars observed by SDSS/SEGUE in the region $r = 14 - 19$ kpc,

reaching a minimum value of -1.2 at $r = 17$ kpc and increasing again. King et al. (2015) also report β values between -2.64 and -0.12 from F-type and BHB stars in the region of $r \sim 12 - 15$ kpc, reaching a minimum (about -4.0) around $r \sim 23$ kpc. Their minimum value, however is much less than that of Kafle et al. (2012), considering both studies including the BHB stars. In any case, the lower value of β reported by all of these studies for the outer halo (the OHR in our case) compared with the inner halo provides strong evidence that the two halos have undergone different assembly histories.

4.2.4. The Impact of Observational Errors

Uncertainties in the observed quantities, such as distance, radial velocity, and proper motions in our sample of stars can result in the derivation of possibly different orbital parameters; hence the structures seen in the map of the anisotropy parameter (left panel of Figure 14) may be distorted by such fluctuations. To assess the impact of the observational uncertainties on the anisotropy parameter, we performed a Monte Carlo simulation to synthesize 100 different samples of our MSTO stars by perturbing the observed distance, radial velocity, and proper motions by an uncertainty of 20% in the distance, and using the quoted uncertainties in the radial velocity and proper motion. We assumed a normal error distribution for our sample.

After generating 100 simulated samples, we computed standard deviations of the rescaled anisotropy parameter (β^*), as shown in the right panel of Figure 14. In the figure, it is clear that the scatter is less than 0.1 in most of the Galactic locations, even though the deviations at the edge of the map become slightly larger because the number of stars becomes smaller. Thus, Figure 14 confirms that there is no large impact on our results and subsequent interpretation arising from uncertainties in the various observed quantities.

5. SPATIAL AND KINEMATIC PROPERTIES OF CEMP-S AND CEMP-NO STARS

We have identified different kinematic properties of the stellar populations in the IHR and OHR from our MSTO sample, which suggest that each halo component likely experienced a different assembly history. We now examine how each of the primary sub-classes of CEMP stars are distributed throughout the halo, and how their kinematic properties differ. The primary reason for this investigation is that the CEMP-*s* and CEMP-no stars are expected to have formed from very different mechanisms, each associated with different ranges of progenitor mass.

It is presently thought that the astrophysical progenitor of CEMP-no stars differs in stellar mass from that of CEMP-*s* stars. The most likely progenitors of CEMP-no stars are “faint supernovae” (or “mixing-and-fallback SNe”) with a mass range of $\sim 20 - 60 M_{\odot}$ (e.g., Umeda & Nomoto 2003, 2005; Nomoto et al. 2013; Tominaga et al. 2014), or “spinstars” with a mass range of $> 60 - 100 M_{\odot}$ (Meynet et al. 2006, 2010; Chiappini 2013). On the other hand, the accepted mechanism to produce the CEMP-*s* stars is binary mass-transfer from low- to intermediate-mass ($1 - 4 M_{\odot}$) asymptotic giant branch (AGB) stars, which can efficiently produce carbon and *s*-process elements. Eventually, the primary AGB star evolves to become a white dwarf, and its secondary com-

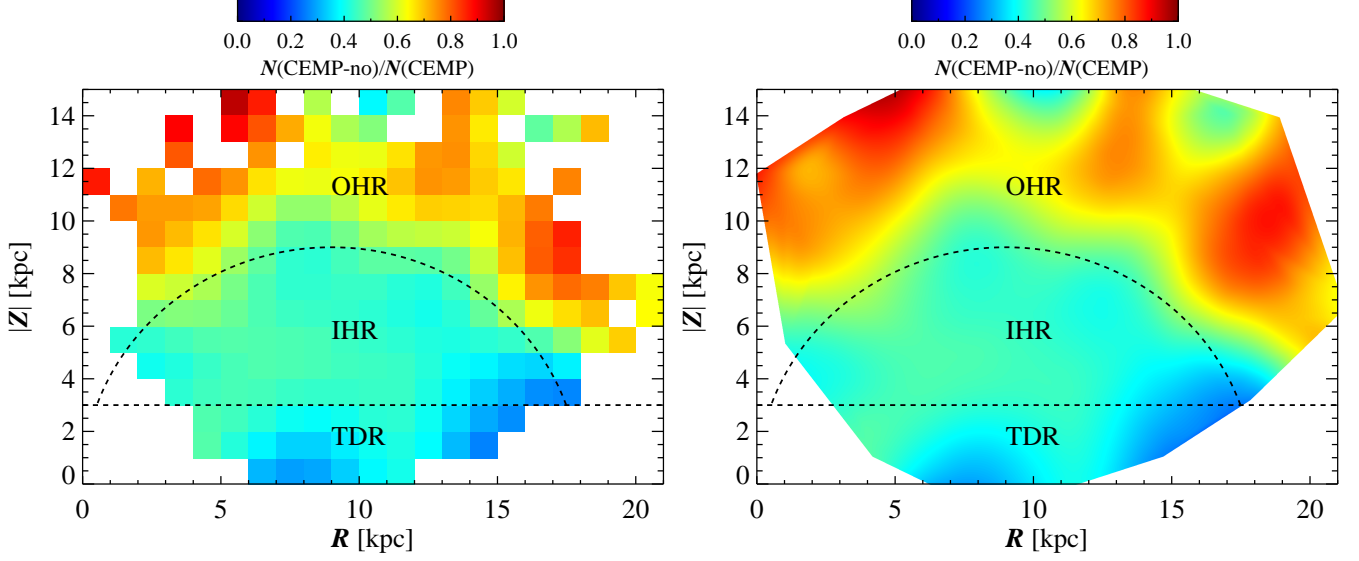


Figure 15. *Left panel:* A map of the ratios of CEMP-no stars relative to the full sample of CEMP stars in our MSTO sample. Following the definition of CEMP stars, we only considered stars with $[\text{Fe}/\text{H}] \leq -1.0$ and $[\text{C}/\text{Fe}] \geq +0.7$. The bin size is 1×1 kpc; each pixel contains at least two stars. A Gaussian kernel has been applied to smooth the distribution. *Right panel:* Same as in the left panel, but with a map produced by interpolating with Quintic polynomials from triangles produced by Delaunay triangulation.

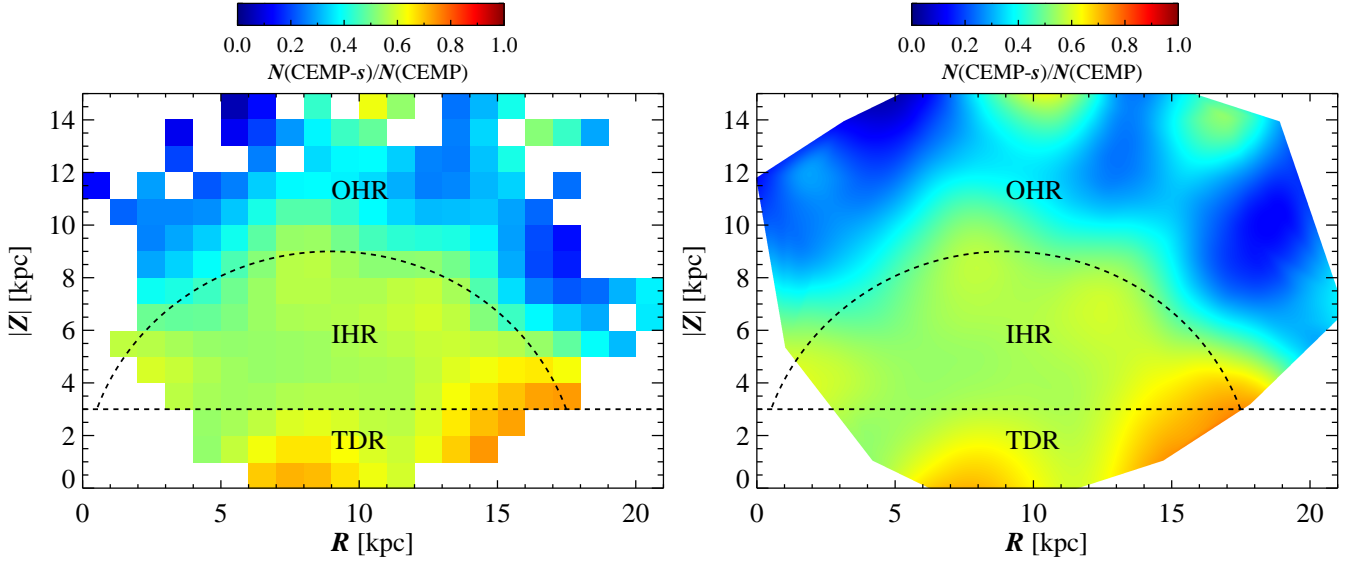


Figure 16. Same as in Figure 15, but for the fraction of CEMP-s stars relative to the full sample of CEMP stars in our MSTO sample.

Table 2
Fractions and Mean Values of $[\text{C}/\text{Fe}]$ for CEMP, CEMP-s, and CEMP-no Stars in each Galactic Region

Region	Fraction			$\langle [\text{C}/\text{Fe}] \rangle$		
	CEMP	CEMP-s	CEMP-no	All	CEMP-s	CEMP-no
TDR	0.031 ± 0.001	0.625 ± 0.024	0.375 ± 0.017	$+0.097 \pm 0.001$	$+1.205 \pm 0.013$	$+0.934 \pm 0.009$
IHR	0.098 ± 0.002	0.560 ± 0.014	0.440 ± 0.012	$+0.259 \pm 0.002$	$+1.175 \pm 0.008$	$+0.932 \pm 0.005$
OHR	0.355 ± 0.016	0.355 ± 0.027	0.645 ± 0.040	$+0.603 \pm 0.013$	$+1.427 \pm 0.043$	$+1.023 \pm 0.014$

Note. — The error in the fraction is derived from Poisson statistics, while the errors listed for $\langle [\text{C}/\text{Fe}] \rangle$ are the standard errors of the mean derived from 100 bootstrapped resamples.

panion is observed as a CEMP-*s* star (e.g., Suda et al. 2004; Herwig 2005; Lucatello et al. 2005; Komiya et al. 2007; Bisterzo et al. 2011; Hansen et al. 2015). As a result, variations in the radial velocity for the surviving star is expected. Strong support for this scenario comes from long-term radial-velocity studies (Starkenburger et al. 2014; Hansen et al. 2016a,b; Jorissen et al. 2016), which report very different binary fractions between these two sub-classes of CEMP stars.

Thus, distinct patterns in spatial distributions and/or kinematics of the CEMP-*s* and CEMP-no stars throughout the halo, if they exist, provide insight to the nature of the environments in which they formed, and their star-formation histories.

Carollo et al. (2014) previously examined the possible association of different CEMP sub-classes with the different stellar populations of the halo, using a small sample ($N \sim 90$) of CEMP stars with available $[C/Fe]$ and $[Ba/Fe]$ estimates obtained from high-resolution spectroscopy. After dividing CEMP stars into likely membership in the IHP and OHP by consideration of their orbital energies, they calculated the fraction of CEMP-no and CEMP-*s* stars in each halo population, finding that the fraction of CEMP-no stars in the OHP is higher, by about a factor of two, than for CEMP-*s* stars, while almost equal fractions of CEMP-*s* and CEMP-no stars were found in the IHP. Yoon et al. (2018) also reported similar fractions of the CEMP-no stars in the IHP and OHP, using subgiant and giant stars from the AEGIS survey. They classified the CEMP stars into the CEMP-*s* and CEMP-no stars by $A(C)$, as adopted in this study. Establishing the validity of these claims requires examination of much larger samples of CEMP stars. We accomplish this by making use of the clear split in the typical levels of $A(C)$ associated with the CEMP-*s* and CEMP-no stars of our MSTO sample, as shown in Figure 2.

Below we first consider the spatial distributions of the relative fractions of CEMP-no to CEMP-*s* stars, and then examine the kinematic properties of each sub-class within each Galactic region.

5.1. Spatial Distribution of CEMP-*s* and CEMP-no Stars

The left panel of Figure 15 shows the fraction of CEMP-no stars relative to the full sample of CEMP stars among our MSTO sample, in the $|Z|$ versus R plane. The right panel is the same as in the left panel, but for a map constructed after interpolating with Quintic polynomials from triangles produced by Delaunay triangulation over the map. This map is for a better visualization of the fractions of the CEMP-no stars in the OHR.

Inspection of these figures immediately reveals two clear results: (1) An increasing fraction of CEMP-no stars as one moves farther into the OHR – more than 60% of the CEMP stars in the OHR are CEMP-no stars, even though there exist a few substructures with relatively higher and lower fractions of CEMP-no stars; and (2) The boundary between the IHR and OHR defined in Figure 1 also clearly divides the two halo regions in terms of lower and higher fractions of CEMP-no stars. A similar map of CEMP-*s* star fractions is shown in Figure 16. As in the CEMP-no map, we note regions with relatively high (and low) fractions of CEMP-*s* stars, as discussed

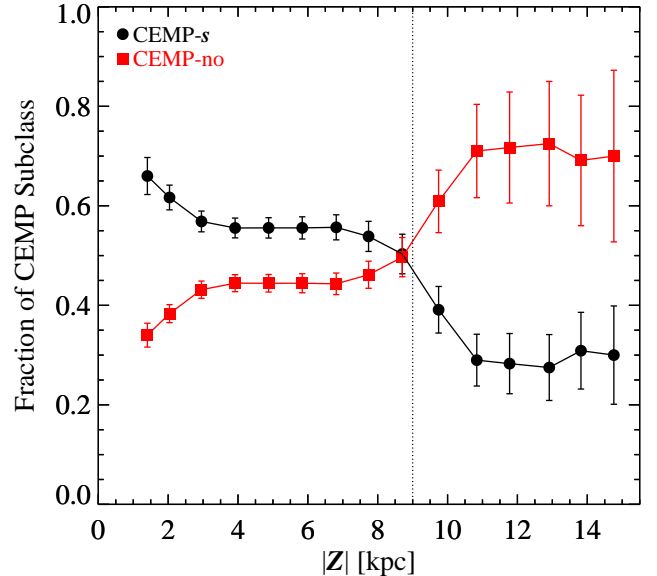


Figure 17. Differential fractions of CEMP-*s* stars (black symbols) and CEMP-no stars (red symbols), as a function of $|Z|$. The bin size is 2 kpc with 1 kpc overlapped with the next neighboring bin. Error bars are derived from Poisson statistics. There is an abrupt increase of CEMP-no stars between $|Z| = 8$ and 11 kpc. The vertical dotted line at $|Z| = 9$ kpc denotes the highest point in the region that separates the IHR from the OHR in Figure 1.

in more detail below. It is noteworthy from inspection of Figures 15 and 16 that the blue (Figure 15) and orange (Figure 16) regions in the range of $13 < R < 18$ kpc and $|Z| < 6$ kpc, indicating relatively large fractions of CEMP-*s* stars, appear to be associated with the Monoceros Stream (Newberg et al. 2002; Ivezić et al. 2008). This suggests that the parent dwarf responsible for the Monoceros Stream has experienced prolonged star formation, consistent with a comparatively high mass.

Quantitatively, we obtained 0.440 ± 0.012 and 0.645 ± 0.040 for the ratio of CEMP-no to CEMP stars for the IHR and OHR, respectively, as listed in Table 2. Our computed ratios confirm that the CEMP-*s* stars in the IHR are favored over the CEMP-no stars, while the CEMP-no stars outnumber the CEMP-*s* by about a factor of two in the OHR, in excellent agreement with the inferred fractions of CEMP-no stars – 0.43 (IHP) and 0.70 (OHP) reported by Carollo et al. (2014), even though we employed a totally different selection criterion for the regions expected to be dominated by stars of the IHP and OHP from theirs. Our derived value of 0.440 for the fraction of the CEMP-no stars in the IHR agrees with that (0.47) of Yoon et al. (2018), while their derived fraction (0.78) of the CEMP-no stars for the OHP is rather higher than ours (0.65).

Taken as a whole, we obtained CEMP frequencies of 0.098 ± 0.002 and 0.355 ± 0.016 for the IHR and OHR, respectively, as listed in Table 2. Among the stars of our MSTO sample, the OHR possesses roughly three times as many CEMP stars as does the IHR, even higher than the contrast reported previously by Carollo et al. (2012).

We also examined the average carbon-to-iron ratios ($\langle [C/Fe] \rangle$) for stars in each Galactic region, as listed in the last three columns of Table 2. Generally, the OHR has a higher $\langle [C/Fe] \rangle$ than the IHR, but the level of the enhancement is not as high as that claimed by Carollo

Table 3
Kinematic Properties in Cylindrical Coordinates for CEMP-*s* and CEMP-no Stars in each Galactic Region

Region	Subclass	N_{tot}	V_R	V_Φ	V_Z	σ_{V_R}	σ_{V_Φ}	σ_{V_Z}	V_Φ	Eccentricity
			(km s ⁻¹)	(km s ⁻¹)	(km s ⁻¹)	(km s ⁻¹)	(km s ⁻¹)	(km s ⁻¹)	(km s ⁻¹)	<i>p</i> -value
TDR	CEMP- <i>s</i>	1067	2.2 ± 4.4	14.6 ± 3.5	2.1 ± 2.4	140.9 ± 3.3	103.5 ± 2.4	81.6 ± 2.3	0.028	0.021
	CEMP-no	640	-2.3 ± 5.2	0.5 ± 3.9	4.0 ± 4.2	129.7 ± 3.1	102.0 ± 3.3	101.5 ± 3.5		
IHR	CEMP- <i>s</i>	2403	-4.8 ± 2.8	-17.4 ± 2.2	3.8 ± 2.0	141.6 ± 1.9	103.0 ± 1.6	104.8 ± 1.5	0.000	0.000
	CEMP-no	1835	-3.8 ± 3.2	-26.4 ± 3.0	0.3 ± 3.0	137.2 ± 2.0	115.6 ± 2.2	112.1 ± 2.0		
OHR	CEMP- <i>s</i>	170	-10.6 ± 10.9	-45.1 ± 8.0	5.4 ± 9.4	150.5 ± 7.6	120.6 ± 6.9	131.2 ± 6.7	0.033	0.015
	CEMP-no	195	-13.5 ± 10.8	-61.5 ± 8.4	4.9 ± 8.3	139.4 ± 6.8	132.6 ± 6.3	117.7 ± 5.8		

Note. — N_{tot} is the total number of stars in each subclass of the CEMP stars. The listed uncertainties are derived from 100 bootstrapped resamples. The *p*-values for V_Φ and eccentricity (*e*) are derived by the K-S two sample test on the distributions of V_Φ and eccentricity (*e*) of the CEMP-*s* and CEMP-no star samples.

Table 4
Kinematic Properties in Spherical Coordinates for CEMP-*s* and CEMP-no Stars in each Galactic Region

Region	Subclass	N_{tot}	V_r	V_θ	V_ϕ	σ_{V_r}	σ_{V_θ}	σ_{V_ϕ}	β
			(km s ⁻¹)	(km s ⁻¹)	(km s ⁻¹)	(km s ⁻¹)	(km s ⁻¹)	(km s ⁻¹)	(km s ⁻¹)
TDR	CEMP- <i>s</i>	1067	2.8 ± 4.8	-1.5 ± 2.5	14.6 ± 3.5	142.7 ± 2.9	78.5 ± 2.7	103.5 ± 2.4	0.586 ± 0.023
	CEMP-no	640	-0.6 ± 5.5	-6.4 ± 3.4	0.5 ± 3.9	132.4 ± 3.8	97.8 ± 2.9	102.0 ± 2.8	0.431 ± 0.040
IHR	CEMP- <i>s</i>	2403	-1.0 ± 2.7	-4.3 ± 1.7	-17.4 ± 2.2	152.4 ± 2.1	88.4 ± 1.7	103.0 ± 1.9	0.603 ± 0.015
	CEMP-no	1835	-0.3 ± 3.5	-3.8 ± 2.1	-26.4 ± 3.0	141.0 ± 2.4	107.3 ± 2.1	115.6 ± 2.1	0.374 ± 0.027
OHR	CEMP- <i>s</i>	170	8.2 ± 12.4	-13.0 ± 10.6	-45.1 ± 8.0	158.8 ± 7.8	120.7 ± 8.9	120.6 ± 7.5	0.423 ± 0.079
	CEMP-no	195	-2.1 ± 9.5	-24.0 ± 8.5	-61.5 ± 8.4	136.7 ± 6.2	119.2 ± 5.8	132.6 ± 6.4	0.150 ± 0.097

Note. — N_{tot} is the total number of stars in each subclass of the CEMP stars. The listed uncertainties are derived from 100 bootstrapped resamples. β is the anisotropy parameter computed by Equation (1).

et al. (2012) ($\langle [C/Fe] \rangle \sim +1.0$ to $+2.0$). As listed in the table, we obtained $\langle [C/Fe] \rangle = +0.259$ and $+0.603$ for the IHR and OHR, respectively. This contrast likely arises due to the fact that we did not restrict our sample by low metallicity ($[Fe/H] < -1.5$) and kinematic properties ($Z_{\text{max}} > 5$ kpc), as was used by Carollo et al., but by the spatial variation of $[C/Fe]$ alone.

We also note that the $\langle [C/Fe] \rangle$ value of the CEMP-no stars is somewhat lower than that of the CEMP-*s* stars for all three regions we considered, implying that the mechanism responsible for producing the CEMP-*s* stars produces more carbon at a given metallicity than that responsible for the CEMP-no stars, as revealed in several previous studies (e.g., Yong et al. 2013; Spite et al. 2013; Bonifacio et al. 2015; Hansen et al. 2016a,b; Yoon et al. 2016, 2018).

The clear association of different CEMP sub-classes with different Galactic halo regions is revealed in Figure 17 as well, which exhibits the differential fractions of CEMP-no (red symbols) and CEMP-*s* (black symbols) stars among CEMP stars in our MSTO sample as a function of $|Z|$. Each bin has a size of 2 kpc with 1 kpc overlapped with the next neighboring bin. Error bars are calculated from Poisson statistics. As in Figure 15, we only consider stars with $[Fe/H] \leq -1.0$ and $[C/Fe] \geq +0.7$.

Figure 17 indicates that there is a very slow increase in the CEMP-no fractions up to $|Z| = 8$ kpc, followed by a steep increase between $|Z| = 8$ and 11 kpc, and an essentially flat behavior at higher $|Z|$. This trend is also well-reflected by the boundaries of the Galactic regions seen in Figures 15 and 16. Consequently, the results from all three figures are clear evidence that the underlying stellar population in the OHR does not share the same

parent population as the IHR.

5.2. Kinematic Characteristics of CEMP-*s* and CEMP-no Stars

We now consider whether or not there exist differences in the kinematic properties for the sub-classes of CEMP stars.

We first examine the average velocity properties of each CEMP sub-class in each Galactic region, as summarized in Table 3 (and in Table 4 for spherical coordinates). According to the tables, in the OHR, the average rotation velocity of CEMP-*s* stars is $\langle V_\Phi \rangle = -45.1 \pm 8.0$ km s⁻¹ and -61.5 ± 8.4 km s⁻¹ for the CEMP-no stars. For the IHR, the mean rotation velocity of CEMP-no stars is lower by about 9 km s⁻¹ than that of CEMP-*s* stars. The general trend is that CEMP-no stars exhibit larger retrograde motions than the CEMP-*s* stars. By comparison with Table 1, which provides kinematic information for the entire sample of our MSTO sample, CEMP stars exhibit lower rotation velocities than carbon-normal stars.

Figure 18 shows the cumulative distribution of rotation velocities (left panels) and orbital eccentricities (right panels) of CEMP-no (red curve) and CEMP-*s* (black curve) stars in each region of the MW. The total number of stars considered in each region is denoted by N_{tot} , shown in the legend of each panel. A non-parametric two-sample K-S test of the distribution of the rotation velocities for CEMP-no and CEMP-*s* stars yields *p*-values of < 0.001 and 0.033 for the IHR and OHR, respectively, as listed in Table 3. It is thus unlikely that the two sub-classes of CEMP stars share the same parent population. Similarly, the *p*-values of < 0.001 and 0.015 for the eccentricity distribution of CEMP-no and CEMP-*s* stars in the IHR and OHR, respectively, reject the hypothesis

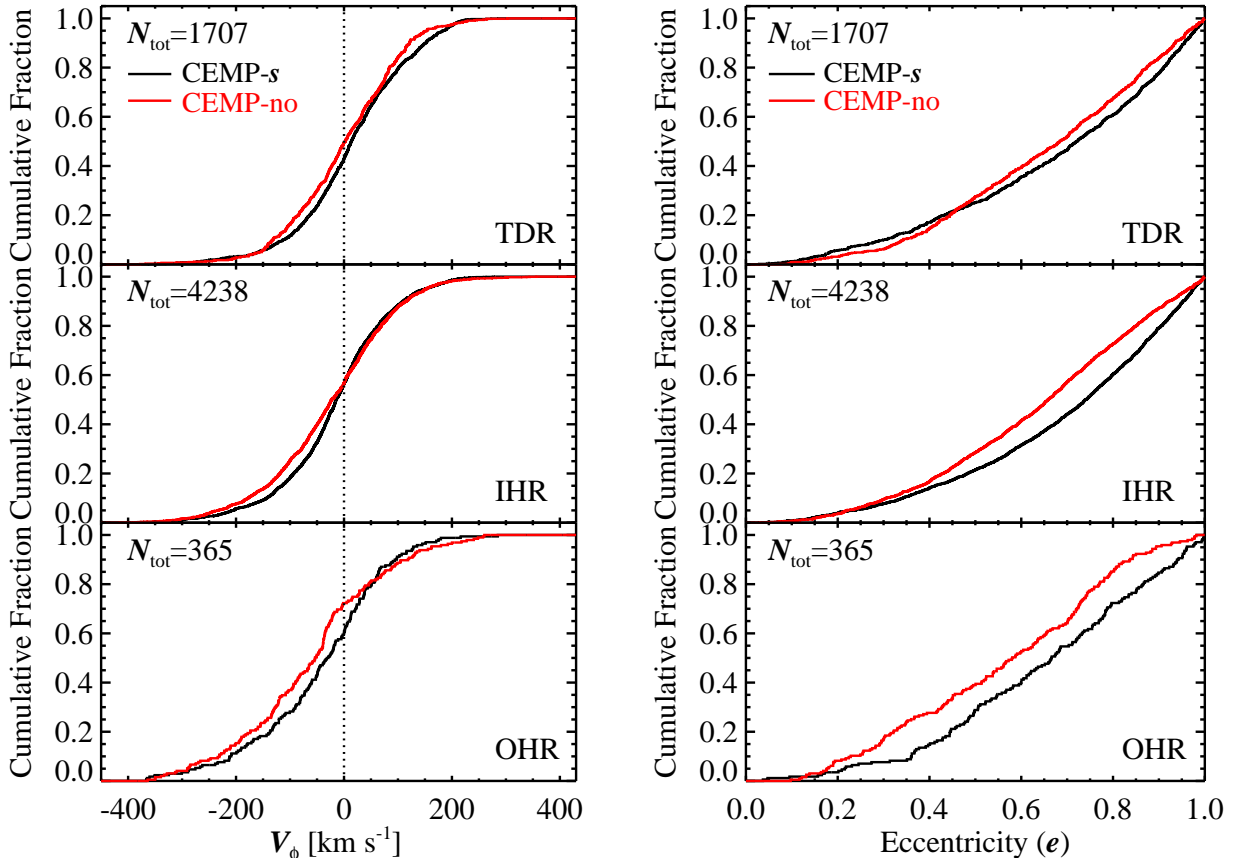


Figure 18. *Left panel:* Cumulative distributions of rotation velocities for CEMP-*s* (black line) and CEMP-no (red line) stars in each Galactic component. The total number of stars considered in each region is denoted by N_{tot} . The vertical dotted line provides a reference at 0 km s^{-1} . *Right panel:* Same as the left panels, but for orbital eccentricities. It is clear that the cumulative distributions in the kinematic properties differ between the CEMP-*s* and CEMP-no stars in the two halo components, indicating that they do not share the same parent population.

of a common parent population.

We also derived the anisotropy parameter for each CEMP sub-class in each halo component, as listed in the last column of Table 4. In the IHR, we obtained $\beta = 0.603$ for the CEMP-*s* stars and 0.374 from the CEMP-no stars; for the OHR, we found $\beta = 0.423$ for the CEMP-*s* stars and 0.150 for the CEMP-no stars. Overall, as $\beta = 0.383$ for the entire sample in the OHR (see Table 1), the CEMP stars in the OHR exhibit a more isotropic distribution of orbits than for the IHR. Within a given halo component, the CEMP-no stars exhibit a more isotropic velocity ellipsoid than the CEMP-*s* stars.

6. INSIGHTS INTO THE FORMATION OF THE GALACTIC HALO

A number of recent cosmological numerical simulations of MW-like galaxies suggest that the inner halos form from mergers of a few relatively massive gas-rich mini-halos, which undergo dissipative collapse while conserving angular momentum (e.g., Zolotov et al. 2009; Font et al. 2011; McCarthy et al. 2012; Tissera et al. 2012, 2013, 2014; Cooper et al. 2015). In these mini-halos, stars that are eventually distributed in the inner halo form continuously to rapidly enrich the interstellar medium. Consequently, the prolonged star formation in such systems lead to the formation of moderately metal-poor stars ($[\text{Fe}/\text{H}] \sim -1.5$), having numerous intermediate-mass ($\sim 1 - 4 M_{\odot}$), which become AGB stars in the late stage of

their evolution. Some of these stars form in a binary system that produce the CEMP-*s* stars observed at present.

In this formation scenario, we can easily understand the higher fraction of CEMP-*s* in the IHR that we identified in Figure 16 and Table 2. Kinematically, this formation mechanism can also naturally explain the higher value of β for the inner halo. The radial velocity component of the stars, which formed out of gas-rich sub-fragments during the dissipative collapse will naturally be enhanced. After merging, these stars would have a flattened distribution, dominated by eccentric orbits.

According to recent theoretical work (e.g., de Binasuti et al. 2014, 2017; Salvadori et al. 2016; Amorisco 2017; Starkenburg et al. 2017), the stellar populations in the outer halos of MW-like galaxies mostly consist of stars that were born in numerous lower-mass mini-halos, and later accreted into the Galactic halo via chaotic, dissipationless mergers. In such low-mass environments, star formation is truncated before forming large numbers of relatively metal-rich, low-mass stars, the dominant source to produce CEMP-*s* stars. As a result, it is expected that there would be more metal-poor ($[\text{Fe}/\text{H}] < -2.0$) and CEMP-no stars formed than CEMP-*s* stars in the Galactic outer halo.

The fact that most CEMP-no stars appear in the regime of $[\text{Fe}/\text{H}] < -2.5$, and the larger fraction of the CEMP-no stars in the OHR, as shown in Figure 15, meet with theoretical expectations, and suggests that the stars

in the OHR were accreted from relatively low-mass dwarf satellites. In addition, since the accreted stars were born in low-mass fragments, they could be easily dispersed by the Galactic tidal force, leading to the formation of a more spherical outer halo. We might expect that the stars from such systems were accreted from all directions, have less eccentric orbits (lower value of the anisotropy parameter), and possibly exhibit counter rotation relative to the inner halo, which was already in place. Once again, these results are commensurate with what we have found for the CEMP-no stars in our MSTO sample. Therefore, from both a chemical and kinematic perspective, we can infer that the stellar population of the OHR is dominated by donated stars from numerous low-mass dwarf satellites.

What kind of dwarf satellites can contribute to the buildup of the Galactic outer halo? The best candidates for such objects are the ultra-faint dwarf (UFD) galaxies around the MW (e.g., [Belokurov et al. 2006a,b](#); [Zucker et al. 2006](#); [Simon & Geha 2007](#), and see [Simon 2018](#) for the current demography of UFDs). In these systems, we expect that star formation occurred early and was stopped or truncated due to the shallow potential well of the systems (e.g., [Brown et al. 2014](#); [Webster et al. 2015](#)). The CEMP-no stars were produced from the nucleosynthetic products of the first burst of the star formation, but not the CEMP-s stars, because the duration of the star formation was not long enough to form the low-mass, relatively high metallicity (> -2.5) AGB stars. Consequently, CEMP-no stars should dominate over CEMP-s stars in such systems. This picture is consistent with our results summarized on [Tables 2, 3, and 4](#), as well as with the relative dominance of CEMP-no stars over CEMP-s stars in the UFDs discovered around the MW (e.g., [Frebel et al. 2014](#); [Frebel & Norris 2015](#); [Frebel et al. 2016](#); [Ji et al. 2016](#)). This inference leads us to conclude that a large fraction of the stars in the OHR were accreted from systems similar to disrupted UFD galaxies. [Yoon et al. \(2019\)](#) also reported the same conclusion that the CEMP-no stars in the Galactic halo were accreted from very low-mass systems such as UFD galaxies by comparing the subgroups of the CEMP-no stars with the CEMP stars found in the dwarf satellite galaxies around the MW.

Additionally, our results suggest that, if all the CEMP-no stars in the outer halo were born in small satellite galaxies such as UFD galaxies that were disrupted into the Galactic halo, we can estimate a lower limit on the fraction of the accreted stars in the outer halo from the ratio of CEMP-no to all CEMP stars. From [Table 2](#), which reports a CEMP-no fraction of 0.645 and a total CEMP fraction of 0.355 for the OHR, we have a fraction of 0.229 (0.645×0.355); hence at least about 23% of the outer-halo stars came from systems such as UFDs.

7. SUMMARY AND CONCLUSIONS

We have examined the chemical and kinematic features of the Galactic halo, making use of over 100,000 MSTO stars from the SDSS. To accomplish, we first divided the halo region into IHR and OHR, based on the varying levels of carbon-to-iron ratios shown in a carbonicity map in the $|Z|$ versus R plane. On average, the stars in the OHR exhibit higher $[C/Fe]$, by about 0.2 dex, than stars in the IHR. We found that the stellar population in the

OHR shows a clear retrograde motion (-49.3 km s^{-1}), with an anisotropy parameter of $\beta = 0.383$, while the population in the IHR exhibits almost no net rotation (-2.6 km s^{-1}) with $\beta = 0.656$. These kinematic differences between the OHR and IHR can be interpreted as arising from the different assembly histories these components experienced.

While analyzing our MSTO stars, we have also investigated the impacts of target-selection bias on our MSTO sample, and found no significant influence on the identification of the Galactic halo regions. We confirmed that our derived distance scale agrees well with that derived from *Gaia* DR2 parallaxes, without any trend evident with respect to $[Fe/H]$, $\log g$, and $[C/Fe]$. The impact of observational uncertainties in the distances, radial velocities, and proper motions on the derived spatial velocities is also small, thus there is no significant influence on the velocity structures revealed by our results arising from these fluctuations.

We further divided the CEMP stars in the IHR and OHR into high- $A(C)$ and low- $A(C)$ stars, which we associate with CEMP-s and CEMP-no stars, respectively, based on the absolute carbon abundance, $A(C)$. First we have mapped the fractions of the CEMP-s and CEMP-no stars in the $|Z|$ and R plane, and found that there are almost twice as many CEMP-no stars than CEMP-s stars in the OHR, while there are almost equal numbers of CEMP-s and CEMP-no stars in the IHR. This information on the different ratios of CEMP-no to CEMP-s stars in the Galactic halo can provide valuable constraints on the mass distributions of the mini-halos from which they formed, as well as their star-formation histories.

We have also examined the kinematic properties for the CEMP-s and CEMP-no stars, and found that the CEMP-no stars exhibit more retrograde motions, and a more isotropic distribution of their orbits, compared to the CEMP-s stars in each halo region. The chemical and kinematic properties found from the MSTO stars indicate that most of the stars in the OHR may be accreted from small satellite galaxies such as the UFD galaxies, as discussed in [Yoon et al. \(2019\)](#). Very conservatively, we estimated from our MSTO stars that at least about 23% of the outer halo stars came from systems such as UFDs, based on the CEMP-no star fraction.

Finally, our work demonstrates ([Figures 12, 13, 14](#), and [Tables 1, 3, and 4](#)) that, even if we separate the halo components based on the spatial distribution of carbonicity, we are able to identify distinct kinematic signatures among the divided halo components, which can provide clues to the origin of the dichotomy of the Galactic halo.

As a third paper in the ‘‘Chemical Cartography’’ series, we are planning to carry out an analysis of kinematic and chemical properties of CEMP giants observed with SDSS, SEGUE, and LAMOST, in order to probe the more distant Galactic halo, and characterize the nature of the dwarf galaxies that contributed stars into the Galactic halo.

We thank an anonymous referee for his/her careful review of this paper to improve the clarity of the presentation.

Funding for SDSS-III has been provided by the Alfred P. Sloan Foundation, the Participating Institutions, the

National Science Foundation, and the U.S. Department of Energy Office of Science. The SDSS-III Web site is <http://www.sdss3.org/>.

The authors thank J. Yoon for reviewing this manuscript and suggesting useful comments to improve this paper. Y.S.L. acknowledges support from the National Research Foundation (NRF) of Korea grant funded by the Ministry of Science and ICT (No.2017R1A5A1070354 and NRF-2018R1A2B6003961). T.C.B. acknowledges partial support for this work from grant PHY 14-30152; Physics Frontier Center/JINA Center for the Evolution of the Elements (JINA-CEE), awarded by the US National Science Foundation, and from the Leverhulme Trust (UK), during his visiting professorship at the University of Hull, when this paper was finished.

REFERENCES

- Allende Prieto, C., Sivarani, T., Beers, T. C., et al. 2008, *AJ*, 136, 2070
- Allende Prieto, C., Fernandez-Alvar, E., Schlesinger, K. J., et al. 2014, *A&A*, 568, 7
- Amorisco, N. C. 2017, *MNRAS*, 464, 2882
- An, D., Beers, T. C., Johnson, J. A., et al. 2013, *ApJ*, 763, 65
- An, D., Beers, T. C., Santucci, R. M., et al. 2015, *ApJ*, 813, L28
- Aoki, W., Beers, T. C., Christlieb, N., Norris, J. E., Ryan, S. G., & Tsangarides, S. 2007, *ApJ*, 655, 492
- Asplund, M., Grevesse, N., Sauval, A. J., & Scott, P. 2009, *ARA&A*, 47, 481
- Bland-Hawthorn, J., & Gerhard, O. 2016, *ARA&A*, 54, 529
- Beers, T. C., Chiba, M., Yoshii, Y., et al. 2000, *AJ*, 119, 2866
- Beers, T. C., & Christlieb, N. 2005, *ARA&A*, 43, 531
- Beers, T. C., Carollo, D., Ivezić, Ž., et al. 2012, *ApJ*, 746, 34
- Beers, T. C., Placco, V. M., Carollo, D., et al. 2017, *ApJ*, 835, 81
- Belokurov, V., Zucker, D. B., Evans, N. W., et al. 2006a, *ApJ*, 642, L137
- Belokurov, V., Zucker, D. B., Evans, N. W., et al. 2006b, *ApJ*, 647, L111
- Belokurov, V., Erkal, D., Evans, N. W., Koposov, S. E., & Deason, A. J. 2018, *MNRAS*, 478, 611
- Bisterzo, S., Gallino, R., Straniero, O., Cristallo, S., & Käppeler, F. 2011, *MNRAS*, 418, 284
- Binney, J., & Tremaine, S. 2008, *Galactic Dynamics* (2nd ed.; Princeton, NJ: Princeton Univ. Press)
- Bond, N. A., Ivezić, Ž., Sesar, B., et al. 2010, *ApJ*, 716, 1
- Bonifacio, P., Caffau, E., Spite, M., et al. 2015, *A&A*, 579, A28
- Brown, T. M., Tumlinson, J., Geha, M., et al. 2014, *ApJ*, 796, 91
- Carollo, D., Beers, T. C., Lee, Y. S., et al. 2007, *Nature*, 450, 1020
- Carollo, D., Beers, T. C., Chiba, M., et al. 2010, *ApJ*, 712, 692
- Carollo, D., Beers, T. C., Bovy, J., et al. 2012, *ApJ*, 744, 195
- Carollo, D., Freeman, K., Beers, T. C., et al. 2014, *ApJ*, 788, 180
- Carollo, D., Beers, T. C., Placco, V. M., et al. 2016, *NatPh*, 12, 1170
- Chen, Y. Q., Zhao, G., Carrell, K., et al. 2014, *ApJ*, 795, 52
- Chen, B. B., Liu, X. W., Yuan, H. B., et al. 2018, *MNRAS*, 476, 3278
- Chiappini, C. 2013, *Astron. Nach.*, 334, 5951
- Chiba, M., & Beers, T. C. 2000, *AJ*, 119, 2843
- Cooper, A., Parry, O. H., Lowing, B., Cole, S., & Frenk, C. 2015, *MNRAS*, 454, 3185
- Cui, X. Q., Zhao, Y. H., Chu, Y. Q., et al. 2012, *RAA*, 12, 1197
- Das, P., & Binney, J. 2016, *MNRAS*, 460, 1725
- Das, P., Williams, & Binney, J. 2016, *MNRAS*, 463, 3169
- Dawson, K. S., Schlegel, D. J., Ahn, C., et al. 2013, *AJ*, 145, 10
- de Bannassuti, M., Schneider, R., Valiante, R. et al. 2014, *MNRAS*, 445, 3039
- de Bannassuti, M., Salvadori, S., Schneider, R. et al. 2017, *MNRAS* 456, 926
- de Jong, J. T. A., Yanny, B., Rix, H.-W., et al. 2010, *ApJ*, 714, 663
- Deason, A. J., Belokurov, V., & Evans, N. W. 2011, *MNRAS*, 411, 1480
- Deason, A. J., Belokurov, V., Koposov, S. E., et al. 2017, *MNRAS*, 470, 1259
- Fernandez-Alvar, E., Allende Prieto, C., Schlesinger, K. J., et al. 2015, *A&A*, 577, 81
- Fernandez-Alvar, E., Allende Prieto, C., Beers, T. C., Lee, Y. S., Masseron, T., & Schneider, D. P. 2016, *A&A*, 593, 28
- Fernandez-Alvar, E., Carigi, L., Allende Prieto, C., et al. 2017, *A&A*, 465, 1586
- Frebel, A., Christlieb, N., Norris, J. E., et al. 2006, *ApJ*, 652, 1585
- Frebel, A., Simon, J. D., & Kirby, E. N. 2014, *ApJ*, 786, 74
- Frebel, A., & Norris, J. E. 2015, *ARA&A*, 53, 631
- Frebel, A., Norris, J. E., Gilmore, G., Wyse, R. F. G. 2016, *ApJ*, 826, 110
- Font, A. S., McCarthy, I. G., Crain, R. A., et al. 2011, *MNRAS*, 416, 2802
- Gaia Collaboration, Brown, A. G. A., Vallenari, A., et al. 2016, *A&A*, 595, 2
- Gaia Collaboration, Brown, A. G. A., Vallenari, A., et al. 2018, *A&A*, 616, 1
- Graczyk, D., Pietrzyński, G., Gieren, W., et al. 2019, *ApJ*, 872, 85
- Gratton, R. G., Carretta, E., Desidera, S., et al. 2003, *A&A*, 406, 131
- Hampel, M., Stancliffe, R. J., Lugaro, M., & Meyer, B. S. 2016, *ApJ*, 831, 171
- Hansen, T. T., Hansen, C. J., Christlieb, N., et al. 2015, *ApJ*, 807, 173
- Hansen, T. T., Andersen, J., Nordström, B., et al. 2016a, *A&A*, 586, 160
- Hansen, T. T., Andersen, J., Nordström, B., et al. 2016b, *A&A*, 588, 3
- Hattori, K., Yoshii, Y., Beers, T. C., Carollo, D., & Lee, Y. S. 2013, *ApJ*, 763, L17
- Helmi, A., Veljanoski, J., Breddels, M. A., Tian, H., & Sales, L. V. 2017, *A&A*, 598, 58
- Helmi, A., Babusiaux, C., Koppelman, H. H., Massari, D., Veljanoski, J., & Brown, A. G. A. 2018, [arXiv:1806.06038](https://arxiv.org/abs/1806.06038)
- Herwig, F. 2005, *ARA&A*, 43, 435
- Hogg, D. W., Blanton, M. R., Roweis, S. T., & Johnston, K. V. 2005, *ApJ*, 629, 268
- Ishigaki, M., Chiba, M., & Aoki, W. 2010, *PASJ*, 62, 143
- Ivezić, Ž., Sesar, B., Jurić, M., et al. 2008, *ApJ*, 684, 287
- Janesh, W., Morrison, H. L., Ma, Z., et al. 2016, *ApJ*, 816, 80
- Ji, A. P., Frebel, A., Ezzeddine, R., Casey, A. R. 2016, *ApJ*, 832, L3
- Jonsell, K., Edvardsson, B., Gustafsson, B., et al. 2005, *A&A*, 440, 321
- Jorissen, A., Van Eck, S., Van Winckel, H., et al. 2016, *A&A*, 586, A158
- Kafle, P. R., Sharma, S., Robotham, A. S. G., et al. 2017, *MNRAS*, 470, 2959
- Kafle, P. R., Sharma, S., Lewis, G. F., & Bland-Hawthorn, J. 2013, *MNRAS*, 430, 2973
- Kafle, P. R., Sharma, S., Lewis, G. F., & Bland-Hawthorn, J. 2012, *ApJ*, 761, 98
- Kawata, D., Bovy, J., Matsunaga, N., & Baba, J. 2019, *MNRAS*, 482, 40
- Kerr, F. J., & Lynden-Bell, D. 1986, *MNRAS*, 221, 1023
- King, C., III, Brown, W. R., Geller, M. J., & Kenyon, S. J. 2015, *ApJ*, 813, 89
- Kinman, T. D., Cacciari, C., Bragaglia, A., Smart, R., & Spagna, A. 2012, *MNRAS*, 422, 2116
- Komiya, Y., Suda, T., Minaguchi, H., et al. 2007, *ApJ*, 658, 367
- Lee, Y. S., Beers, T. C., Sivarani, T., et al. 2008a, *AJ*, 136, 2022
- Lee, Y. S., Beers, T. C., Sivarani, T., et al. 2008b, *AJ*, 136, 2050
- Lee, Y. S., Beers, T. C., Allende Prieto, C., et al. 2011, *AJ*, 141, 90
- Lee, Y. S., Beers, T. C., Masseron, T., et al. 2013, *AJ*, 146, 132
- Lee, Y. S., Beers, T. C., Kim, Y. K., et al. 2017, *ApJ*, 836, 91
- Lindgren, L., Hernández, J., Bombrun, A., et al. 2018, *A&A*, 616, 2
- Lucatello, S., Tsangarides, S., Beers, T. C., et al. 2005, *ApJ*, 625, 825
- Lucatello, S., Beers, T. C., Christlieb, N. C., et al. 2006, *ApJ*, 652, L3
- McCarthy, I. G., Font, A. S., Crain, R. A., et al. 2012, *MNRAS*, 420, 2245
- Meynet, G., Ekström, S., & Maeder, A. 2006, *A&A*, 447, 623

- Meynet, G., Hirschi, R., Ekstrom, S., et al. 2010, *A&A*, 521, 30
- Mints, A., & Hekker, S. 2019, *A&A*, 621, 17
- Nandakumar, G., Schultheis, M., Hayden, M., et al. 2017, *A&A*, 606, 97
- Newberg, H. J., Yanny, B., Rockosi, C., et al. 2002, *ApJ*, 569, 245
- Nissen, P. E., & Schuster, W. J. 2010, *A&A*, 511, L10
- Nissen, P. E., & Schuster, W. J. 2011, *A&A*, 530, 15
- Nomoto, K., Kobayashi, C., & Tominaga, N. 2013, *ARA&A*, 51, 457
- Placco, V. M., Frebel, A., Beers, T. C., Stancliffe, R. J. 2014 *ApJ*, 797, 21
- Prugniel, Ph., & Soubiran, C. 2001, *A&A*, 369, 1048
- Rossi, S., Beers, T. C., & Snenen, C. 1999, in *ASP Conf. Ser.* 165, Third Stromlo Symposium: The Galactic Halo, eds. B. Gibson, T. Axelrod, & M. Putman (San Francisco: ASP), 264
- Salvadori, S., Skuladottir, A., de Bressana, M. 2016, *AN*, 337, 935
- Santucci, R. M., Beers, T. C., Placco, V. M., et al. 2015, *ApJ*, 813, 16
- Scannapieco, C., White, S. D. M., Springel, V., & Tissera, P. 2009, *MNRAS*, 396, 696
- Schlesinger, K. J., Johnson, J. A., Rockosi, C. M., et al. 2012, *ApJ*, 761, 160
- Schönrich, R., Binney, J., & Dehnen, W. 2010, *MNRAS*, 403, 1829
- Schönrich, R., Asplund, M., & Casagrande, L. 2011, *MNRAS*, 415, 3807
- Schönrich, R., Asplund, M., & Casagrande, L. 2014, *ApJ*, 786, 7
- Schönrich, R., McMillan, P., & Eyer, L. 2019, *MNRAS*, 487, 3568
- Simon, J. D., & Geha, M. 2007, *ApJ*, 670, 313
- Simon, J. D. 2018, *ApJ*, 863, 89
- Smith, M. C., Evans, N. W., Belokurov, V., et al. 2009, *MNRAS*, 399, 1223
- Smolinski, J. P., Lee, Y. S., Beers, T. C., et al. 2011, *AJ*, 141, 89
- Spite, M., Caffau, E., Bonifacio, P., et al. 2013, *A&A*, 552, A107
- Starkenbug, E., Shetrone, M. D., McConnachie, A. W., & Venn, K. A. 2014, *MNRAS*, 441, 1217
- Starkenbug, E., Oman, K. A., Navarro, J. F., et al. 2017 *MNRAS*, 465, 2212
- Suda, T., Aikawa, M., Machida, M. N., & Fujimoto, M. Y. 2004, *ApJ*, 611, 476
- Tian, H., Liu, C., Xu, Y., et al. 2019, *ApJ*, 871, 184
- Tissera, P. B., White, S. D. M., & Scannapieco, C. 2012, *MNRAS*, 420, 255
- Tissera, P. B., Scannapieco, C., Beers, T. C., & Carollo, D. 2013, *MNRAS*, 432, 3391
- Tissera, P. B., Beers, T. C., Carollo, D., & Scannapieco, C. 2014, *MNRAS*, 439, 3128
- Tominaga, N., Iwamoto, N., & Nomoto, K. 2014, *ApJ*, 785, 98
- Umeda, H., & Nomoto, K. 2003, *Nature*, 422, 871
- Umeda, H., & Nomoto, K. 2005, *ApJ*, 619, 427
- Webster, D., Bland-Hawthorn, J., & Sutherland, R. 2015, *ApJ*, 799, L21
- Wojno, J., Kordopatis, G., Piffl, T., et al. 2017, *MNRAS*, 468, 3368
- Yanny, B., Newberg, H. J., Johnson, J. A., et al. 2009, *AJ*, 137, 4377
- Yong, D., Norris, J. E., Bessell, M. S., et al. 2013, *ApJ*, 762, 27
- Yoon, J., Beers, T. C., Placco, V. M., et al. 2016, *ApJ*, 833, 20
- Yoon, J., Beers, T. C., Dietz, S., et al. 2018, *ApJ*, 861, 146
- Yoon, J., Beers, T. C., Tian, D., & Whitten, D. D. 2019, *ApJ*, 878, 97
- York, D. G., Adelman, J., Anderson, J. E., Jr., et al. 2000, *AJ*, 120, 1579
- Zolotov, A., Willman, B., Brooks, A. M., et al. 2009, *ApJ*, 702, 1058
- Zucker, D. B., Belokurov, V., Evans, N. W., et al. 2006, *ApJ*, 643, L103